9-12-2014

Statistical Analysis of High-Order Moments from Direct Numerical Simulation of a Turbulent Boundary Layer

Bryan Kaiser

Bryan E. Kaiser

Candidate

Mechanical Engineering

Department

This thesis is approved, and it is acceptable in quality and form for publication:

Approved by the Thesis Committee:

Dr. Svetlana V. Poroseva, Chairperson

Dr. C. Randall Truman

Dr. Peter Vorobieff

Dr. Daniel Appelö

Statistical Analysis of High-Order Moments from Direct Numerical Simulations of a Turbulent Boundary Layer

by

Bryan E. Kaiser

B.S., Mechanical Engineering, University of New Mexico, 2013
B.F.A., Concentration in Painting, Alfred University, 2006

THESIS

Submitted in Partial Fulfillment of the
Requirements for the Degree of

Master of Science
Mechanical Engineering

The University of New Mexico

Albuquerque, New Mexico

July, 2014

Dedication

To anyone who finds inspiration in nature.

Acknowledgments

I thank my advisor, Dr. Poroseva, for the vision, insight, and mentorship she provided throughout the duration of this project. I also thank her for encouraging me to pursue research, giving me the opportunity to publish a journal paper, the millions of recommendation letters she has sent on my behalf, and her support throughout many research projects in the last few years.

I thank my committee for not only for being on my committee but also for being my teachers. The enjoyment I find in computational fluid dynamics is rooted in the courses I took from you.

I thank Juan Sillero and the Universidad Politécnica de Madrid Fluid Dynamics Group for generously sharing data. I also thank Juan for the time and energy he spent answering my questions regarding this project.

I thank Elsa Castillo from the School of Engineering student services office. Without Elsa's tireless effort to increase the scholarship opportunities available to engineering students, I would not have completed my BSME and would certainly not have written this thesis.

I thank Mary Beth Libbey for technical writing tutoring and Carl Kaiser for copy editing this thesis.

I thank my parents, my brothers, and my partner Frances, for their love and support during my time at engineering school.

Statistical Analysis of High-Order Moments from Direct Numerical Simulations of a Turbulent Boundary Layer

by

Bryan E. Kaiser

B.S., Mechanical Engineering, University of New Mexico, 2013
B.F.A., Concentration in Painting, Alfred University, 2006

M.S., Mechanical Engineering, University of New Mexico, 2014

Abstract

High-order zero-pressure-gradient turbulent boundary layer statistics are important for turbulence modeling efforts and insight into the nature of turbulent flow. In this thesis, a complete database of third-, fourth-, and fifth-order central velocity moments is presented. The statistics were extracted from flow field data from a finely resolved direct numerical simulation by the Universidad Politécnica de Madrid Fluid Dynamics Group. Fourth-order moment interrelations formed by invoking Millionshtchikovs hypothesis of quasinormality and fifth-order moment interrelations formed by utilizing truncated Gram-Charlier series expansions of the marginals of the joint probability density function of the flow are presented. Reasonable agreement was found for most of the moment interrelations. Flow visualizations using the Q criterion are also presented.

Contents

List of Figures

List of Tables

Glossary

Re_θ	Reynolds number based on momentum thickness, $\theta U_\infty/\nu$.
u_τ	friction velocity, $\sqrt{\nu \partial U/\partial y}$.
$\tilde{u}, \tilde{v}, \tilde{w},$	total streamwise, wall-normal, and spanwise velocities.
u^+, v^+, w^+	central streamwise, wall-normal, and spanwise velocity moments (fluctuations). Nondimensionalized by u_τ.
U^+, V^+, W^+	mean streamwise, wall-normal, and spanwise velocities. Nondimensionalized by u_τ.
x^+, y^+, z^+	streamwise, wall-normal, and spanwise distances. Nondimensionalized by ν/u_τ.
δ^+	von Kármán number: $\delta u_\tau/\nu$ boundary layers, $0.5hu_\tau/\nu$ channels.
δ	0.995 of the boundary layer thickness.
δ^*	boundary layer displacement thickness.
θ	boundary layer momentum thickness.
ν	kinematic viscosity.

Chapter 1

Introduction

1.1 The Turbulent Boundary Layer

The complexity of turbulence is represented mathematically by the Navier-Stokes equations. The nonlinear advection terms in the equations generate random velocity and pressure fluctuations in turbulent flows. In a turbulent boundary layer, kinetic energy from the free-stream flow is transferred into velocity and pressure fluctuations in the boundary layer and then is dissipated in the boundary layer by viscosity. However, fluid dynamicists continue to struggle to explain the mechanisms that produce the turbulent fluctuations, how energy is dissipated in the boundary layer, how the different layers within the turbulent boundary layer interact, and what role the structures (i.e. coherent motions) play in dynamics of the boundary layer.[1]

Sir Osbourne Reynolds was the first fluid dynamicist to decompose a turbulent field into mean and fluctuating components.[2] Reynolds showed that by substituting the decomposed quantities into the Navier-Stokes equations an unclosed system of equations is formed, known today as the Reynolds-averaged Navier-Stokes (RANS)

equations.[3] The equations for mean velocity include ensemble-averaged velocity fluctuation terms referred to as Reynolds stresses, which are representative of the coupling between the turbulent fluctuations and the mean field.

An incompressible zero-pressure-gradient (ZPG) turbulent boundary layer on a flat plate is considered the canonical turbulent boundary layer. It is expected that if this flow is completely understood, it will shed light on the dynamics of more complicated turbulent boundary layers that include curved surfaces, pressure gradients, large free-stream turbulent fluctuations, injection/suction, and other complex flows. In an incompressible ZPG turbulent boundary layer, the profile of the mean streamwise velocity is used to identify several layers, each associated with its own dynamical processes, as shown for a moderate Reynolds number in Figure 1.1. The "+" notation for the velocity U signifies nondimensionalization by the friction velocity u_τ and the same notation for the wall normal coordinate signifies nondimensionalization by ν/u_τ.

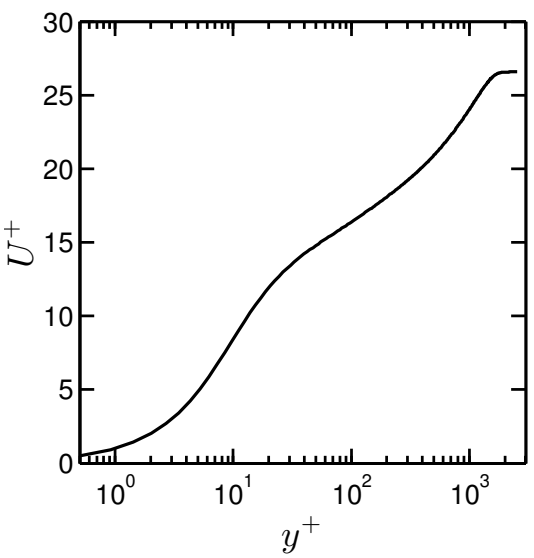

Figure 1.1: Mean streamwise velocity at $Re_\theta = 5200$

Closest to the wall is the viscous sublayer, where the effects of the fluid's inertia and the pressure gradient are small, and viscous effects are dominant. Moving away from the wall, the next region is known as the buffer layer, which features anisotropic distributions of distinct pockets of high and low fluid velocities.[1] The buffer layer contains the location of the peak turbulent kinetic energy production within the boundary layer[4,3,5] and the location of maximum turbulence intensity for moderate Reynolds numbers.[6,5] The next layer is the logarithmic (log) layer, which is named after a theoretical logarithmic expression for mean velocity that includes empirically determined coefficients called the log law. High Reynolds number turbulent boundary layers may be defined as containing logarithmic regions of appreciable length.[5] In this region the effects of viscosity on turbulent fluctuations are negligible. Finally, the outermost region of the turbulent boundary layer is referred to as the wake region or outer layer.[3,7] The outer layer is characterized by large eddy structures that form a wavy interface between turbulent and irrotational parts of the flow, and the outer layer entrains mass and momentum from the free-stream.[8]

1.2 Motivation

Turbulent boundary layers appear in many engineering applications. However, turbulent flows contain a wide range of time and length scales and so directly simulating the governing equations of turbulent flows requires massive computational resources. The goal of turbulence modeling is to create models that accurately predict turbulent flows using limited computational resources. Turbulence modelers strive to predict variables relevant to engineering applications, such as an object's drag coefficient, and to reduce the number of floating point operations that must be performed.

Reynolds stress transport (RST) turbulence models are an attractive type of turbulence model for engineering applications because they simulate turbulent flows using less computational resources than direct numerical simulation (DNS) and large eddy simulation (LES), and they produce more accurate results than first-order turbulence closure models. RST models are second-order RANS turbulence models. Like the first-order RANS equations, the RST equations are unclosed.

One modeling approach for closure is to generate closure terms using empirical functions. However, the accuracy of an empirical function depends on how similar the computed flow is to the flow used to generate the empirical function. The higher the order of turbulence closure, the more sensitive the modeled terms are to the dynamics of the specific flow. Therefore, empirical functions lack universality and may introduce significant errors. In addition, the modeled terms of RST equations include high-order mixed moments that are difficult to measure by experiment.

Another modeling approach for closure is to analyze the physics of the flow and generate a mathematical statement through physical reasoning. An example of physical reasoning in turbulence modeling is the correct assertion that the effect of random velocity fluctuations on turbulent flows closely resembles the effect of thermal agita-

tion of molecules on the movement of gases, known as the concept of eddy viscosity or turbulent viscosity. Unfortunately, physical analysis of higher-order closure terms is exceedingly difficult, but empirical functions and physical analysis are not the only tools available to the turbulence modeler. Statistical tools may be employed to construct closure terms from known variables. Closure schemes that employ statistical tools promise more universality than empirical functions and more tractability than physical reasoning.

1.3 Objectives

The complete statistical description of the evolution of near-wall turbulence behavior is far from being obtained.[3] In this thesis, LES and DNS are considered as tools for collecting high-order turbulence statistics to add to the statistical description of turbulent boundary layers. The primary goals of this thesis are 1) to extract high-order statistical moments from flow field data of a turbulent boundary layer and 2) to evaluate the validity of central moments constructed using Gram-Charlier series expansions for the probability distributions of turbulent quantities[9,6] and to evaluate the validity of central moments constructed using Millionshtchikov's hypothesis of quasi-normality in the fluctuating components of the turbulent boundary layer velocity field.[10]

This thesis is organized as follows: an overview of simulation types is provided in Chapter 2. Chapter 3 discusses an unsuccessful attempt to collect turbulence statistics by LES and the collection technique used for extracting turbulence statistics from DNS data. Chapter 4 presents the turbulence statistics from DNS data and the constructued central moments, and conclusions are drawn in Chapter 5.

Chapter 2

Simulation of Turbulent Boundary Layers

2.1 Direct Numerical Simulation

Numerical solutions to the Navier-Stokes equations for turbulent conditions are referred to as direct numerical simulation. DNS was unattainable until the 1970s, when the amount of memory and processing speed of the most advanced computers could finally accommodate the wide range of length and time scales present in a turbulent flow. In the last 40 years DNS has matured into a research tool for examining geometrically simple turbulent flows such as jets, pipe flows, channel flows, wakes, and boundary layers, to name a few. Verified and validated DNS data is considered experiment-quality and provides a more detailed portrait of the flow field than is possible through experiments.[11] Conceptually, DNS is the simplest type of turbulent flow simulation, but the wide range of scales present in turbulent flows requires fine grid resolution and therefore extensive computational resources.

For accurate DNS of turbulent flows, the spatial scales, from the integral scales to the Kolmogorov scales, must be resolved. The integral scale is a spatial measure of the largest possible eddy in the flow, and it is essentially the distance over which the fluctuating component of the velocity remains correlated. An eddy is loosely defined as a turbulent motion characterized by a timescale, lengthscale, and characteristic velocity. Each linear dimension of the computational domain must be at least a few times larger than the integral scale. The smallest resolved lengthscale, the Kolmogorov scale η, imposes the fine grid resolution requirement for DNS and consequently the computational expense.

Kolmogorov hypothesized that at high Reynolds numbers, the small-scale turbulent motions are statistically isotropic (the turbulent fluctuations are of equal magnitude in all directions).[12] Kolmogorov further hypothesized that smallest eddies receive energy from larger eddies at the same rate as the smallest eddies dissipate heat, and so the motion at the smallest scale depends only on the rate of the supply of energy, equal to the dissipation rate ϵ, and the kinematic viscosity of the fluid Although Kolmogorovs hypotheses do not account for the presence of intermittency (pockets of irrotational flow at all scales in turbulent flows), grid resolution of a lengthscale of $O(\eta)$ is widely considered a sufficient resolution criterion for accurate DNS of turbulent flows.[11] The assumption that the Kolmogorov lengthscale is the smallest relevant lengthscale inherently assumes that the Kolmogorov lengthscale is much larger than the mean free path of the molecules in the fluid, i.e. the continuum hypothesis is valid.[3]

The physical motions captured by a simulation are functions of the grid resolution and the numerical methods employed to discretize derivatives and interpolate values. Generally speaking, a higher-order accurate spatial discretization may use fewer grid points for the same flow resolution as a lower-order accurate spatial discretization on more grid points. The error of spatial discretization schemes has two sources:

differentiation error, which is an estimate of how well the discretization scheme resolves the derivatives of the flow, and error associated with the nonlinearity of the Navier-Stokes equations.[11,13] The differentiation error as a function of the resolution of a wave may be estimated by matching the differentiation stencil with a truncated Taylor series or by Fourier analysis of the velocity field.

The error associated with the nonlinearity of the Navier-Stokes equations is most significant at the small scales. The nonlinearity of the equations causes the interaction of scales smaller than the grid resolution and scales at and above grid resolution. Intuitively, if the Kolmogorov scales are resolved the error will be small. If the nonlinear spatial derivatives are represented as Fourier modes (i.e. a set of basis functions), the nonlinear operations will generate higher modes than those represented by the set.[11,13] Therefore, the nonlinearity of the equations produces contributions from higher-order modes that are improperly added to the set of basis functions. The error from this process is referred to as aliasing, and it must be considered when implementing discretization schemes.[11,13]

There are three common approaches to discretization of the Navier-Stokes equations: the finite difference method (FDM), the finite volume method (FVM), and the finite element method (FEM). For the FDM, the partial derivatives of the governing equations are approximated in terms of the nodal values of the functions. The result is one algebraic equation per grid node. The FDM is arguably the simplest discretization scheme to implement but it is difficult to implement on unstructured grids (grids composed of non-parallelepiped cells) and the method does not conserve mass flux through the computational domain without the addition of a constraint.[13]

The FVM discretizes the integral form of the Navier-Stokes equations. As its name implies, the computational domain is divided into smaller control volumes, and the surface and volume integrals of the governing equations are approximated using quadrature. The FVM conserves mass flux through the domain without addi-

tional constraints and it is suited to any type of grid, but implementing the FVM in three-dimensions is more difficult to program than FDM because differentiation, integration, and interpolation schemes must implemented for all dimensions.[13]

The FEM also uses the integral form of the governing equations, but what distinguishes it from the FVM is the multiplication of weight functions to the integrands computed for each of the discrete volumes, or elements, within the domain. The FEM is relatively easy to analyze mathematically and use for complex geometries, but the matrices of the linearized equations are often not well structured, so it can be challenging to find efficient computational methods for FEMs.[13]

The wide range of time scales present in turbulent flows must be resolved by time advancement schemes for DNS. Large timesteps may cause numerical instability for explicit time advancement of DNS of constant-density incompressible flow. How large is too large a timestep is revealed by the Courant condition for incompressible flows, as shown in Equation 2.1.

$$\frac{u\Delta t}{\Delta x} < \alpha \tag{2.1}$$

Here, α is a parameter that depends on the particular selected time advancement scheme and u is a characteristic velocity. The logic of the Courant condition is that a simulation will become unstable if a fluid parcel moves across a cell in less time than the simulation advances.

Since the Navier-Stokes equations include only a first-order time derivative, time advancement schemes are numerical solutions to ordinary differential equations (ODEs). Problems featuring wide ranges of time scales are called stiff and are the most challenging ODEs to solve.[11] Third- and fourth-order Runge-Kutta schemes are common time advancement schemes. For incompressible flow, the speed of sound is infinite and consequently pressure cannot be computed explicitly. The fractional step method of Kim & Moin[14] is a popular method for implicitly solving for the pressure and en-

forcing continuity. A review of common time advancement schemes may be found in Ferziger.[13]

Inducing and sustaining a turbulent boundary layer in DNS is challenging because of the computational constraints on domain size. Simulating transition from laminar to turbulent flow requires a large computational domain and the tripping mechanism for the transition adds complexity to the simulation. A common alternative to simulating transition to turbulence is to employ a turbulent inflow method.

It is an ongoing challenge to construct a turbulent inflow method such that the turbulent fluctuations at the inlet plane possess physically accurate phase relationships and anisotropy. Spalart & Leonard[15] created one of the first turbulent inflow methods. They proposed a coordinate transformation of the Navier-Stokes equations that represents the turbulent boundary layer in a statistically homogenous manner in the streamwise direction. The result permits the use of periodic boundary conditions, so that the simulation generates its own turbulent inflow, as well as the use of a highly accurate Fourier series representation of the velocity field in the streamwise direction. However, their method is complicated and difficult to program. Lund *et al.*[16] proposed a much simpler "modified Spalart method" that does not require a coordinate transformation of the Navier-Stokes equations and instead rescales the mean and fluctuating quantities at a downstream recycle station using a single empirical relation and feeds the information to the upstream inlet plane. Their method is arguably the most popular turbulent inflow method used for DNS and LES. For a detailed review of the multitude of turbulent inflow methods the reader is referred to Sagaut.[17]

If the error introduced by the turbulent inflow method at the inlet plane is minimal, then turbulent fluctuations consistent with the dynamics of the Navier-Stokes equations are reconstructed by nonlinear effects as the flow progresses in the streamwise direction. Once the maxima of the fluctuation intensities (the peak fluctuating

quantities divided by their respective mean quantities) has reached what appear to be asymptotic gradual growth rates, the reconstruction of the turbulent fluctuations is complete.[8] The streamwise length over which the reconstruction occurs, after enough time for the initial flow conditions to pass completely out of the domain, is known as the adaptation length. The adaptation length may be measured by an approximation of the distance that the largest eddies in the flow are advected, known as the eddy turnover length, L_{to}, expressed in Equation 2.2.[18]

$$L_{to} = \frac{U_\infty \delta_{99}}{u_\tau} \tag{2.2}$$

A non-dimensional turnover distance for the adaptation length, $\tilde{x}$, may be calculated by integrating the streamwise distance of the adaption length divided by the turnover length, expressed in Equation 2.3.[18]

$$\tilde{x} = \int_0^x \frac{u_\tau}{U_\infty \delta_{99}} dx \tag{2.3}$$

The significant computational expense of DNS forbids its use as an engineering tool and restricts its use to investigating relatively simple flows of moderate Reynolds number. As shown in Figure 2.1, the Reynolds number based on momentum thickness θ of many practical flows is often several orders of magnitude larger than what is possible to simulate by DNS, and high-quality experiments require expensive facilities.[19] Some groups have argued that the observed Reynolds number dependence of turbulence statistics is purely a consequence of which quantities are chosen for non-dimensionalization, commonly referred to as scaling variables.[11] However, Reynolds number dependence and appropriate scaling variables are topics of ongoing debates that require more extensive explanations than can be provided here. For simplicity, conventional inner and outer scaling variables are used in this thesis. The reader is referred to DeGraaff & Eaton,[7] George & Castillo[20], Monkewitz *et al.*,[21] Panton,[22] and Wei *et al.*.[23] for more information regarding the new scaling variables.

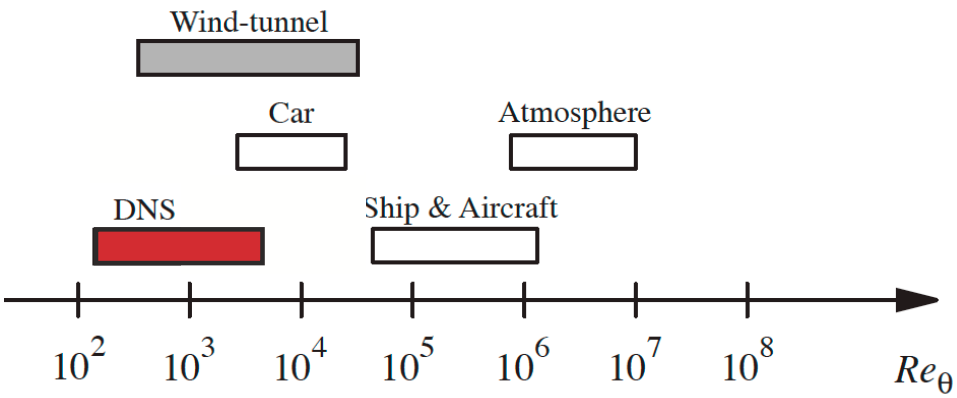

Figure 2.1: Re_θ ranges for various applications

2.2 Large Eddy Simulation

Large eddy simulation is a useful tool for collecting flow field information from flows that are too computationally expensive to simulate by DNS. As the name implies, the largest eddies are simulated directly and the smallest eddies are modeled. The level of approximation of the flow may be split into two components: the level of space-time resolution and the level of dynamic description. The gap between the smallest relevant scales simulated without modeling and the Kolmogorov scales is a measure of the space-time resolution. The required level of space-time resolution for a flow depends on what information is sought. The selected level of dynamic description is determined by judging the relative importance of the various forces acting on the primitive variables. For example, all of the turbulent boundary layer simulations described in this document simulate perfectly isothermal, incompressible flows of Newtonian fluids, which are, strictly speaking, unrealistic. The differences between the simulated flows and real flows with infinitesimal variations in temperature and viscosity due to such assumptions are negligible in most cases. However,

neglected dynamics in the subgrid turbulence models that describe the turbulence of the unresolved scales, also known as the subgrid scales, are often significant. The dynamics that are modeled are often flow-specific, and the interested reader is referred to Kassinos *et al.*[24]

The governing equations of explicit LES feature additional terms that account for the evolution of the flow at the subgrid scales. The mathematical filtering of the flow into resolved and unresolved quantities is misleadingly similar in form to Reynolds decomposition. For Reynolds decomposition, the mean of the fluctuating quantities is zero by definition, but for LES the mean of the unresolved quantities is not necessarily zero. The concept of subgrid viscosity is also distinct from the concept of turbulent viscosity because its corresponding lengthscale is grid-dependent. One popular subgrid scale turbulence model is the subgrid-viscosity model of Germano *et al.*[25] The model is a turbulence closure scheme, based on the local resolved scales, that is composed of an equation for the subgrid scale stresses and a subgrid scale kinematic viscosity relation. For more information on subgrid models and explicit LES, the reader is referred to Saguat.[17] For implicit LES, extra terms are not introduced into the governing equations. Instead, complex numerical methods are chosen that effectively cancel the numerical error of the computations with the resolution error of the grid.

Boundary conditions and the turbulent inflow methods for LES are similar to those for DNS. Both DNS and LES may be computed in physical space or Fourier (spectral) space. In Fourier space, the spatial variations of the primitive variables are represented as a truncated series of orthogonal basis functions. Computations in Fourier space are more efficient because the basis functions are global, so the solutions for all points are computed in the same operation. The drawbacks of computing the flow field in Fourier space are that it is more challenging to compute in parallel and that periodic boundary conditions must be used.

2.3 Reynolds-Averaged Navier-Stokes Simulation

In general, engineering applications of computational fluid dynamics do not require a complete description of the evoloution of the flow field. Instead, engineers are often interested solely in mean quantities. A computationally affordable alternative for an engineer using a desktop computer is to solve for the one-point moments of the flow field using a truncated set of the RANS equations. The RANS equations are formed by using Reynolds decomposition to average the flow, as in Equation 2.4-Equation 2.6. The turbulent quantities are decomposed into mean and fluctuating components, the bar notation indicates averaging, and the index i is used for Einstein notation of the velocity vector components.

$$\tilde{u}_i = U_i + u_i, \quad \tilde{p} = P + p, \tag{2.4}$$

$$\overline{\tilde{u}_i} = U, \quad \overline{\tilde{p}} = P, \tag{2.5}$$

$$\overline{u_i} = 0, \quad \overline{p} = 0. \tag{2.6}$$

The decomposed quantities are substituted into the Navier-Stokes equations, and the raw moments of the Navier-Stokes equations are formed, as in Equations 2.7 and 2.8.

$$\frac{\partial U_i}{\partial t} + U_j \frac{\partial U_i}{\partial x_j} = -\frac{\partial P}{\partial x_i} - \frac{\partial \overline{u_i u_j}}{\partial x_j} + \nu \frac{\partial^2 U_i}{\partial x_j^2}, \tag{2.7}$$

$$\frac{\partial U_i}{\partial x_i} = 0. \tag{2.8}$$

The system of mean velocity equations in Equations 2.7 and 2.8 is unclosed without an additional equation for the Reynolds stress, $\overline{u_i u_j}$, generated by the non-linear terms in the Navier-Stokes equations. By taking the raw moment of the first central moments and the raw moment of the Navier-Stokes equations, a transport equation for $\overline{u_i u_j}$ is generated. The transport equation for $\overline{u_i u_j}$ is known as the

Reynolds stress transport equation and it includes a new obstacle for closure, the third-order central moment $\overline{u_i u_j u_k}$. By taking the raw moment of increasingly high-order central moments and the Navier-Stokes equations, an infinite set of RANS equations may be formed. Equations 2.9 and 2.10 show operation which generates the RST equation. Equations 2.11 and 2.12 show the operations that generate the third- and fourth-order central moment transport equations.

$$N(\tilde{u}_i) = \frac{\partial \tilde{u}_i}{\partial t} + \tilde{u}_j \frac{\partial \tilde{u}_i}{\partial x_j} + \frac{\partial \tilde{p}}{\partial x_i} - \nu \frac{\partial^2 \tilde{u}_i}{\partial x_j^2}, \tag{2.9}$$

$$\overline{u_i N(\tilde{u}_j) + u_j N(\tilde{u}_i)} = 0, \tag{2.10}$$

$$\overline{u_i u_j N(\tilde{u}_k) + u_i u_k N(\tilde{u}_j) + u_j u_k N(\tilde{u}_i)} = 0, \tag{2.11}$$

$$\overline{u_i u_j u_k N(\tilde{u}_l) + u_i u_j u_l N(\tilde{u}_k) + u_i u_k u_l N(\tilde{u}_j) + u_j u_k u_l N(\tilde{u}_i)} = 0. \tag{2.12}$$

A complete set of RANS equations yields a complete statistical description of the evolution of a turbulent flow field.[26] However, the system of equations must be truncated for computation; therefore, some terms must be modeled for closure. The order of the closure scheme corresponds to highest order moments that are solved for at all grid points, i.e. a first-order RANS closure scheme generates solutions for only the mean quantities.

Typical first-order closure strategies involve a transport equation for turbulent kinetic energy, which is derived by taking the trace of the RST equation. All of the terms in the turbulent kinetic energy transport equation have a firm physical basis. However, another equation representing the evolution of turbulent lengthscales is required for first-order closure schemes. Transport equations for the dissipation rate of turbulent kinetic energy, eddy viscosity, and other surrogate quantities for the turbulent lengthscale are commonly used for one- and two-equation RANS closure schemes. The number of equations in the description of a RANS closure refers to the number of transport equations of turbulent quantities. A thorough review of common one- and two-equation RANS closure schemes may be found in Wilcox.[27]

Spalart[28] defined two principal challenges for turbulence modeling: I) accurate prediction of the growth and separation of turbulent boundary layers, and II) accurate prediction of momentum transfer after separation. Simulations of first-order RANS closure schemes can achieve limited accuracy for challenge I flows and are inaccurate for challenge II flows.[28] A significant source of error arises from the empirical functions employed throughout first-order closure schemes. Empirical functions are not universal to all flows by the nature of their formulation. Furthermore, it has been shown analytically that for some wall-bounded flows first-order closure schemes cannot accurately predict mean velocity components.[29]

Second- and higher-order closure schemes offer improved descriptions of challenge I and II, compared with first-order closures, and include more statistical detail. Higher-order closure terms are more difficult to model with empirical functions[28] because it is more difficult to collect the relevant data from experiments, and the behavior of higher-order closure terms is more sensitive to the specific flow. However, it has been demonstrated that statistical tools for describing random fields can be used to formulate higher-order moments in terms of lower-order moments.[6,30] Turbulent velocity fields are known to be approximately Gaussian at individual points in the flow but do not constitute Gaussian random fields. The marginals of a three-dimensional joint probability density function, describing a close-to-Gaussian turbulent velocity field, may be approximated as Gram-Charlier series expansions.[9] By truncating the series expansions, higher-order mixed velocity moments may be equated to sums and products of lower-order mixed velocity moments. Similar formulations may be generated by using the Millionshtchikov's hypothesis of quasi-normality in the fluctuating components of the velocity field.[10] High-order central moment interrelations are discussed in section 5.3 and 5.4.

2.4 Other Types of Simulations

In recent years, several new types of simulations have been developed. Notable examples include unsteady Reynolds-averaged Navier-Stokes (URANS) simulations, detached eddy simulation (DES), and quasi-direct numerical simulation (QDNS). In contrast to RANS simulations, which inherently assume that the flow is steady, URANS simulations advance the flow in time and capture only fluctuations with lower frequencies (larger time scales) than the time step used for advancement. DES is a hybrid of RANS simulation and LES techniques that uses the RANS equations in regions of the flow where the turbulent scales are very small. QDNS is essentially very finely resolved LES that employs a subgrid scale model for viscous stress alone. A complete review of URANS, DES, and QDNS is not possible here, and the reader is referred to Speziale[31] for more information regarding URANS, Spalart[28] regarding QDNS, and Spalart[32] regarding DES.

Chapter 3

Generation of Turbulent Statistics

Two attempts were made to collect high-order turbulent statistics. The first attempt involved modifying the High Gradient hydrodynamics code (HIGRAD), an LES code written by researchers at Los Alamos National Laboratory, for simulation of a ZPG turbulent boundary layer. The second attempt involved post-processing the data of a DNS of a ZPG turbulent boundary layer to collect the desired statistics.

3.1 LES using the High-Gradient Hydrodynamics Code of Los Alamos National Laboratory

HIGRAD is an atmospheric computational fluid dynamics code created by Los Alamos National Laboratory to accurately represent flows characterized by sharp gradients in velocity, concentration, and temperature. HIGRAD uses a fully compressible finite-volume formulation for explicit LES and features an advection scheme that is second-order accurate in time and space. HIGRAD includes a grid transformation from the simulation grid to a fully orthogonal computational grid of constant

resolution.[33] The grid transformation reduces the error associated with numerical discretization of the governing equations onto irregular grids of topography. HIGRAD has been used to simulate a wide variety atmospheric phenomena including hurricanes, flow over urban areas, explosive dispersion, and coupled wind turbine/atmosphere processes.[34,35]

FIRETEC is a multi-phase transport wildfire model that couples with HIGRAD. Within FIRETEC is a subgrid model that contains turbulence closure equations. It includes a Reynolds stress tensor model based on the Boussinesq approximation,[27] turbulent kinetic energy transport equations, and a subgrid-viscosity model, all of which are represented on three subgrid scales.[36]

HIGRAD was selected as a potential tool for generating high-order turbulent statistics because data from finely resolved LES may closely approximate data from DNS. However, to modify HIGRAD for simulation of a ZPG turbulent boundary layer over a flat plate eight modifications were required. The required modifications and the progress made towards achieving them are presented in the list below.

1. *Modification of Grid Transformation Scales.*
   The grid transformation scheme within HIGRAD permitted a minimum cell dimension of 1 m. This was changed to allow a minimum grid dimension of $1 \cdot 10^{-7} m$.

2. *Implementation of a Wall Boundary Condition.*
   As an atmospheric CFD tool, HIGRAD uses a permeable solid boundary condition at the wall to model the effect of vegetation on atmospheric flows. A Dirchlet boundary condition was used to set the velocity components at the wall to zero, and a Neumann boundary condition was used to set the derivative of the pressure at the wall to zero.

3. *Implementation of a Boundary Condition at the Top of the Domain for a ZPG.*
   To maintain a ZPG, the simulation domain height must be much greater than the boundary layer height or a lower domain height may be used in conjunction with a special top boundary condition. For the latter, the boundary condition at the top of the domain must allow a unit mass equal to that contained within a unit volume with the height of the displacement thickness to exit. To implement the condition, a Neumann boundary condition must be implemented for the streamwise and spanwise velocity components (Equation 3.1) and a streamwise function (Equation 3.2) must be implemented for the wall-normal velocity.[16,18]

$$\frac{\partial \tilde{u}}{\partial y} = \frac{\partial \tilde{w}}{\partial y} = 0, \tag{3.1}$$

$$\tilde{v} = U_\infty \frac{\partial \delta^*}{\partial x}. \tag{3.2}$$

   Neuman boundary conditions that set the wall-normal derivatives of all velocities to zero were implemented in HIGRAD and the computational domain heights were a minimum of 20 boundary layer thicknesses.

4. *Implementation of a Turbulent Inflow Method and Convective Exit Boundary Conditions.*
   As discussed in Chapter 2, simulating transition to turbulence is computationally demanding for both DNS and LES. In addition, simulating transition to turbulence requires special subgrid models. Alternatively, turbulent inflow generation methods attempt to produce turbulent fluctuations at the inlet plane that possess accurate phase relationships and anisotropy. A turbulent inflow method was not introduced, but the modified Spalart method by Lund *et al.*,[16] which rescales the exit velocities using an empirical function for the friction velocity, was selected as a potential candidate. However, to implement the method of Lund *et al.*[16] the discretized equations and their associated numerical schemes must be converted from compressible to incompressible forms.

5. *Turbulent Flow Initialization.*

   The flow fields were initialized using mean velocity profiles from simulations of similar Reynolds number and a random turbulent intensities from 0 to 0.1 superimposed uniformly on the mean profiles. If an appropriate amount of time elapses, it has been shown that this is an acceptable initialization procedure.[16]

6. *Addition of Viscous Diffusion to the Governing Equations.*

   Viscous diffusion terms were added by adding a constant kinematic viscosity to the subgrid model terms in the resolved momentum equations. The modification added a viscous diffusion term to the resolved scales alone.

7. *Modification of the FIRETEC Subgrid Model to a Conventional Subgrid Viscosity Model.*

   As mentioned previously, to collect high-order statistics using LES the computational grid resolution must approach the resolution requirements for DNS. As the grid becomes finer, the effect of the subgrid model on the resolved scales decreases. The FIRETEC subgrid model was modified to compute one subgrid scale, with no combustion, for an isothermal flow.

8. *Implementation of an Incompressibility Condition and Appropriate Discretization Methods.*

   To avoid compressiblity effects the computed flows were of a Mach number of 0.3 or less.[37] However, the addition of unneccessary equations and terms potentially introduce an additional source of numerical error and present an additional challenge for implementing a turbulent inflow method. Optimally, HIGRAD would be converted to computing incompressible flow, but numerical schemes for compressible flows are quite different than those for incompressible flows and the task of converting HIGRAD into an incompressible flow-solver is non-trivial.

Given the significant amount of required code modifications presented above and a project timescale of one year, the attempt to simulate a high-fidelity ZPG turbulent boundary layer was abandoned in favor of utilizing data from an existing DNS of a ZPG turbulent boundary layer.

3.2 DNS by the UPM Fluid Dynamics Group

The Universidad Politécnica de Madrid (UPM) Fluid Dynamics Group generously provided velocity and pressure fields from their DNS of a ZPG turbulent boundary layer flow over a flat plate for the extraction of high-order turbulent statistics. A precursor low-resolution simulation, referred to as BL_{AUX}, was used to minimize the flow development distance and generate a turbulent flow field passed to the inlet of the main high-resolution simulation, BL_{6600}. The UPM group used the method of Lund *et al.*[16] for BL_{AUX}, so it generated its own turbulent inflow from a recycle location. A location towards the back of the computational domain of BL_{AUX} was sampled for the inflow of BL_{6600}. The turbulent flow field was passed from BL_{AUX} to BL_{6600} by making three adjustments. The first was to interpolate the flow field to fit the node locations of the BL_{6600} grid, the second was to extend the area of free stream flow upwards to match the taller height of BL_{6600}, and the third modification was to slightly adjust the passed turbulent field to enforce constant mass flux inflow for BL_{6600}. The domain of BL_{6600} extends from $Re_\theta = 2780$ to 6680 in the streamwise direction, and the ratio of the domain height to the boundary layer thickness at the exit plane is approximately 2.5. The physical orientation of BL_{AUX} and BL_{6600} from Sillero *et al.*[18] is shown in Figure 3.1.

Periodic spanwise boundary conditions and convective exit boundary conditions were used for both computational domains. The primitive-variable formulation of the incompressible Navier-Stokes equations was solved using a fractional step method[14]

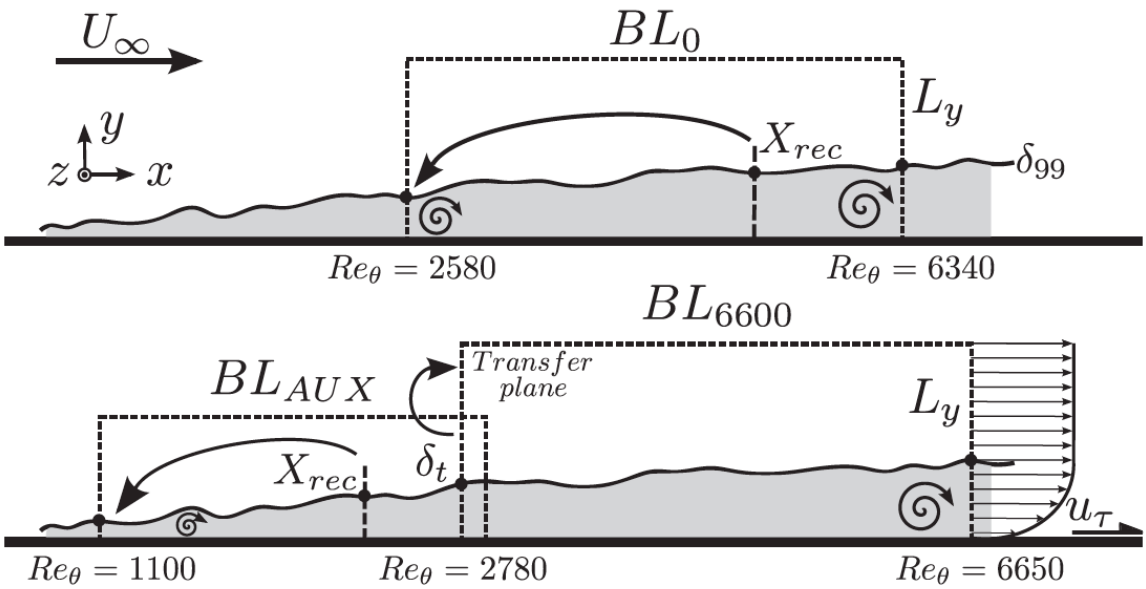

Figure 3.1: Boundary layer simulation schematic

to ensure mass conservation. Spatial derivatives in the streamwise and wall-normal directions were computed using staggered three-point compact finite differences[38] with the exception of the Poisson equation for pressure, which was computed with centered second-order finite differences. Staggered Cartesian grids, shown in Figure 3.2 as drawn in Simens *et al.*,[39] were introduced by Harlow & Welch[40] and allow for straightforward evaluation of the mass fluxes in the continuity equation due to the location of the velocities on the cell faces.

Compact finite difference schemes, such as Padé schemes, can be derived by fitting polynomials to the velocity profile across several nodes. Unlike traditional finite differences, compact finite differences use the derivatives of the velocity profile as well as the velocity profile to derive coefficients for a matching polynomial.[38] The advantage of compact finite difference schemes is that they require fewer nodes for the computation of derivatives compared with central finite differences. A Fourier spectral representation was used for the variables in the spanwise direction, dealiased

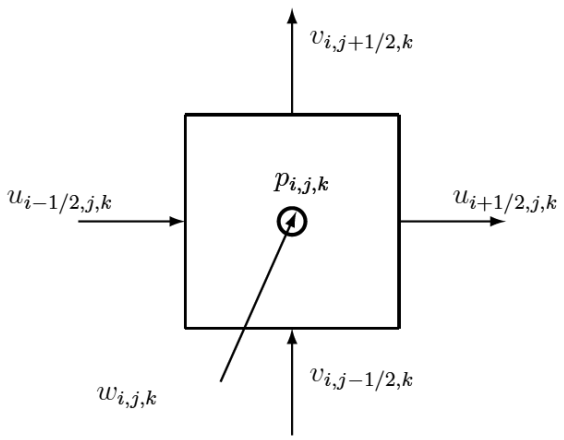

Figure 3.2: BL_{6600} staggered grid

using the 2/3 rule. Time was advanced using a semi-implicit, three-step Runge Kutta scheme. The reader is referred to Simens *et al.*[39] regarding further numerical method details, and to Borrell *et al.*[41] for code parallelization details.

Chapter 4

Analysis of Turbulent Statistics

4.1 Interpolation and Ensemble Averaging

High-order turbulence statistics were collected at streamwise locations corresponding to $Re_\theta = 4101$ and 5200 ($\delta^+ = 1331$ and 1626). It was determined in Sillero *et al.* that all relevant flow scales in BL_{6600} are correctly represented for $Re_\theta > 4800$. However, statistical comparisons with experiment data were deemed acceptable as low as $Re_\theta > 4101$ because was shown by Sillero *et al.*[18] that the maximum Reynolds stress, δ/θ, and the wake intensity are close to convergence at $Re_\theta = 4101$. In addition, the second-order statistics collected by a hot wire anemometry (HWA) experiment by Schwarz[42] at the same Reynolds number possess up to 15% uncertainty. Turbulence statistics were obtained using over 200 statistically independent flow realizations taken from the simulation after an initial washout period for a total time period of approximately 11.5 turnover times of the largest turbulent eddy, defined as $t = \delta/u_\tau$.[18] Statistics were ensemble averaged over the spanwise direction and the streamwise direction for a short region in which the change in the boundary layer thickness is less than 1.22%.

The formal order of accuracy of a simulation is the lowest order numerical scheme implemented in the code.[39] As the UPM Group implemented a centered second-order finite difference scheme to solve the Poisson equation, the data is formally second-order accurate.[39] Fourth-order compact finite differences schemes[38] were implemented to compute derivatives in the streamwise and wall-normal directions in the simulation. A fourth-order interpolation scheme was employed to interpolate the data and collocate the staggered grid for statistical analysis. An algorithm created by Fornberg[43] for approximating the derivatives of a variable was used as a computationally efficient procedure for polynomial interpolation.

The Lagrange interpolation formula[44] states that the unique interpolation polynomial, $p(x)$, interpolates the total velocity $\tilde{u}(x_i)$ at distinct node locations x_i, where $i = 1 : n$ is expressed by Equations 4.1 and 4.2.

$$l_j(x) = \prod_{i=1}^{n} \frac{x - x_i}{x_j - x_i}, j = 1 : n, i \neq j, \tag{4.1}$$

$$p(x) = \sum_{j=1}^{n} \tilde{u}(x_j) l_j(x). \tag{4.2}$$

To approximate the behavior of the k^{th} derivative at a given x location, Fornberg[43] stated Equation 4.3.

$$\frac{d^k \tilde{u}(x)}{dx^k} \approx \frac{d^k p(x)}{dx^k}. \tag{4.3}$$

The weights ${c_j}^k$ may then be found by substituting recursion relations for Lagrange polynomials into a Taylor series approximation of the previous equation.[43] Once the weights are found, the polynomial of the k^{th} order derivative may be computed for a given location (Equation 4.4).[43] The zeroth derivative is an interpolation.

$$\frac{d^k p(x_j)}{dx^k} = \sum_{j=1}^{n} c_j^k u(x_j). \tag{4.4}$$

4.2 Statistical Tools for Closure Schemes

Once the staggered streamwise and wall-normal velocities were collocated the random pressure and velocity fields were decomposed by Reynold's decomposition into mean and fluctuation components, as shown in chapter 2. The mean quantity is also referred to as the statistical expectation or raw moment of a random variable, and the fluctuating quantities are the first central moments, shown in Equations 4.5 and 4.6.[45]

$$(\tilde{u} - U)^n = u^n, \tag{4.5}$$

$$\overline{u^0} = 1, \qquad \overline{u^1} = 0, \qquad \overline{u^2} \geq 0. \tag{4.6}$$

The second central moment is known as the variance and is the square of the standard deviation. Standardized moments are higher-order central moments nondimensionalized by the variance and raised to one half the order of the corresponding central moment.[45] The third- and fourth-order standardized moments, shown in Equations 4.7 and 4.8, are known as the skewness and flatness factors, respectively.

$$S_u = \frac{\overline{u^3}}{\overline{u^2}^{3/2}}, \tag{4.7}$$

$$F_u = \frac{\overline{u^4}}{\overline{u^2}^2}. \tag{4.8}$$

The sign of the skewness factor indicates the direction of a shift in the peak of a Gaussian probability distribution. A Gaussian probability distribution is symmetric about zero for central moments, so $S = 0$ for Gaussian probability distributions. The flatness factor is a measure of the thickness of the tails of the distribution, and for a Gaussian distribution the flatness factor is $F = 3$.[45]

If all of the statistics of a random field are invariant under a shift in time, it is statistically stationary. Similarly, if all of the statistics of a random field are

invariant under a shift in space, it is statistically homogenous.[45] The theorem of ergodicity states that if a random field is statistically stationary and homogenous then indefinitely repeated sampling from a single probe will produce the same results as a single sample from a large number of probes.[17] Since the considered ZPG turbulent boundary layer is statistically homogenous in the spanwise direction and statistically stationary in time, the theorem of ergodicity permits spatio-temporal averaging to increase the size of the statistical sample. In addition, a limited distance in the streamwise direction may also be used to increase the sample because the flow is approximately homogenous for a distance that corresponds to a change in boundary layer height of less than 1.22%. Equations 4.9-4.11 express the ensemble averaging for third-, fourth-, and fifth-order mixed moments.

$$\overline{u_i u_j u_k} = \frac{1}{N_z N_t N_x} \int_{z_0}^{z} \int_{t_0}^{t} \int_{x_0}^{x} (\tilde{u}_i - U_i)(\tilde{u}_j - U_j)(\tilde{u}_k - U_k) dz dt dx, \tag{4.9}$$

$$\overline{u_i u_j u_k u_l} = \frac{1}{N_z N_t N_x} \int_{z_0}^{z} \int_{t_0}^{t} \int_{x_0}^{x} (\tilde{u}_i - U_i)(\tilde{u}_j - U_j)(\tilde{u}_k - U_k)(\tilde{u}_l - U_l) dz dt dx, \tag{4.10}$$

$$\overline{u_i u_j u_k u_l u_m} = \frac{1}{N_z N_t N_x} \int_{z_0}^{z} \int_{t_0}^{t} \int_{x_0}^{x} (\tilde{u}_i - U_i)(\tilde{u}_j - U_j)(\tilde{u}_k - U_k)(\tilde{u}_l - U_l)(\tilde{u}_m - U_m) dz dt dx. \tag{4.11}$$

As mentioned in chapter 2, the DNS data evaluated in this thesis is used to examine the validity of higher-order central moments constructed from lower-order central moments for second- and higher-order RANS model closures. Currently, there are two approaches to construct higher-order central moments constructed from lower-order central moments based on considering statistical properties of a turbulent flow field. The first approach, as shown by Fériet[9] begins by writing the boundary layer transport equations for central moments starting from the conservation laws, as shown below in Equations 4.12 and 4.13.

$$\frac{1}{n+1}\frac{\partial\overline{u_i^{n+1}}}{\partial t}+\frac{U_j}{n+1}\frac{\partial\overline{u_i^{n+1}}}{\partial x_j}+\overline{u_i^n u_j}\frac{\partial U_i}{\partial x_j}+\frac{1}{n+1}\frac{\partial\overline{u_i^{n+1}u_j}}{\partial x_j}-\overline{u_i^n}\frac{\partial\overline{u_i u_j}}{\partial x_j}=\overline{u_i^n(\nu\frac{\partial^2 u_i}{\partial x_j^2}-\frac{\partial p}{\partial x_i})}, \tag{4.12}$$

$$\Omega_i=\overline{u_i^n(\nu\frac{\partial^2 u_i}{\partial x_j^2}-\frac{\partial p}{\partial x_i})}. \tag{4.13}$$

For steady wall-bounded flows, the three-dimensional joint probability distribution, $P_j(u_j, v, \Omega_i)$, may be introduced. The marginals of the joint probability distribution are Equations 4.14 and 4.15.

$$P_{i1}(u_i, v)=\int_{-\infty}^{\infty}P_i(u_i, v, \Omega_i)d\Omega_i, \tag{4.14}$$

$$P_{i2}(u_i, \Omega_i)=\int_{-\infty}^{\infty}P_i(u_i, v, \Omega_i)dv. \tag{4.15}$$

In a non-Gaussian turbulent velocity field, as in most turbulent flows of industrial interest, Gram-Charlier series expansions (a series expansion using orthonormal functions in the form of Hermite polynomials) may be used to represent the marginals of the joint probability distribution.[9] The first terms of the expansion correspond to a Gaussian probability distribution and the remaining terms in the expansion express deviations from a Gaussian distribution.[6] By truncating the expansion, it was shown that alternative sets of equations for the interrelations of the moments may be derived.[6,30] The fourth- and fifth-order interrelations of the high-order moments obtained by truncating Gram-Charlier expansions are shown below in Equations 4.16-4.18.

$$\overline{u_i^5}=10\,\overline{u_i^2}\,\overline{u_i^3}, \tag{4.16}$$

$$\overline{u_i^4u_j}=6\,\overline{u_i^2}\,\overline{u_i^2u_j}+4\overline{u_iu_j}\,\overline{u_i^3}, \tag{4.17}$$

$$\overline{u_i^2u_j^3}=6\,\overline{u_iu_j}\,\overline{u_iu_j^2}+\overline{u_i^2}\,\overline{u_j^3}+3\overline{u_i^2u_j}\,\overline{u_j^2}. \tag{4.18}$$

The Gram-Charlier series expansion procedure is applicable to fourth- and higher-order statistical turbulence closures and its validity was successfully tested in boundary layer flow experiments, such as, the turbulent boundary layer on a flat plate,[30,46,47] and an open-channel flow over smooth and rough surfaces.[48] Good agreement between experimental data[49,50] and those obtained using the Gram-Charlier series expansion technique was also observed in a cylindrical pipe flow.[51,52] The second procedure uses Millionshtchikovs hypothesis of quasinormality.[10] The quasinormality hypothesis is used in third-order statistical closures and is based on the assumption of Gaussian distribution of a turbulent velocity field for fourth- and higher-order velocity correlations. The validity of this hypothesis was demonstrated for one-point statistics in experiments by Uberoj[53] and for two-point statistics by Zaets.[54] In the turbulent boundary layer, Equations 4.19 and 4.20 relate the central velocity moments.

$$\overline{u_i^3 u_j} = 3\,\overline{u_i u_j}\,\overline{u_i^2}, \tag{4.19}$$

$$\overline{u_i^2 u_j^2} = 2\,\overline{u_i u_j}\,\overline{u_i u_j} + \overline{u_i^2}\,\overline{u_j^2}. \tag{4.20}$$

Chapter 5

Results

The one-point, first- and second- order moments (i.e. the mean velocities and Reynolds stresses) extracted from BL_{6600} at $Re_\theta = 5160$ are discussed in detail by Sillero *et al.*[18] They presented additional validation information, and the reader is referred to Sillero *et al.*[18] for more information regarding the validation of lower-order moments.

5.1 Third-, Fourth-, and Fifth-Order Moments

The reported statistics constitute the first complete DNS database of third- to fifth-order velocity central moments in turbulent boundary layers. Figures 5.1 to 5.38 plot the behavior of the third-order central velocity moments throughout the turbulent boundary layer at streamwise locations corresponding to $Re_\theta = 4101$ and 5200. The bar notation is used to signify the ensemble averaging discussed in Chapter 3. The plots are shown with conventional inner and outer scaling dimensions y^+ and y/δ, respectively. Blue lines correspond to data extracted at $Re_\theta = 4101$ and the red lines correspond to data extracted at $Re_\theta = 5200$.

Third-order moment validation data from hot wire anemometry (HWA) measurements at $Re_\theta = 4101$ by Schwarz,[42] laser doppler velocimetry (LDV) measurements at $Re_\theta = 5200$ by DeGraaff,[55] HWA measurements at $Re_\theta = 4980$ by Smith & Schwartz,[56] and HWA measurements $Re_\theta = 4850$ by Klewicki[57] are depicted by $\bullet$, $\times$, $\triangle$, and $+$, respectively. Verification DNS data from a simulation by Schlatter & Örlü[58] is shown by $\bigcirc$.

The BL_{6600} results and experiment data are in general agreement, except for velocity moments that contain higher powers of the wall-normal velocity fluctuation such as $\overline{v^3}^+$ and $\overline{uv^2}^+$. For the HWA results, the discrepancy may be explained by the difficulty of measuring central moments of the wall-normal velocity with one hot wire directly adjacent to the other.[7] It has also been noted that size of the hot wire may mask or expose the statistical footprints of different structures, determined by the size of the hot wire.[59] Although the hot wire measurements of Schwarz[42] are recorded only in the outer region of the turbulent boundary layer, the statistical footprint of smallest wall-normal fluctuations (i.e. Kolmogorov eddies $\eta \approx 1.5\delta_v$) may be filtered out by the large size of the hot wire. The characteristic non-dimensional length for a hot wire is $L^+ = Lu_\tau/\nu$, where L is the active length of the wire. Table 5.1 shows a comparison of the spatial resolution of BL_{6600} and wire resolution of the HWA experiment by Schwarz.

Data	δ_v	$\Delta y^+, L^+$
BL_{6600}	$0.0074m$	0.32
Schwarz (HWA)	$0.000015m$	83.90

Table 5.1: Resolution Comparison at $Re_\theta = 4101$

The skewness factors indicate significant departures from Gaussian distribution in the viscous sublayer and outer region for streamwise and wall-normal velocity fluctuations. The large quantity of positive wall-normal fluctuations in those regions,

shown by the experiment data as well as the DNS data, may contribute to the HWA experiment spatial resolution error in the outer region.

Schlatter & Örlü[58] also used a version of the Lund *et al.*[16] turbulent inflow generation method, but they computed all primitive variables in Fourier space. Table 5.2 compares the spatial resolution of BL_{6600} to the spatial resolution of the LDA by DeGraaff.[55] The spatial resolution error of the LDA by DeGraaff[55] is comparable to that of the UPM Fluid Dynamics Group's DNS and therefore does not explain the difference between the DNS data and the LDA data. The difference could be explained by an overprediction of the friction velocity in the experiment by DeGraaff.[55]

Data	δ_v	Δy^+	Δz^+
BL_{6600}	$0.0076m$	0.32	4.07
DeGraaff (LDA)	$0.000021m$	1.65	2.83

Table 5.2: Resolution Comparison at $Re_\theta = 5200$

Fourth- and fifth-order central velocity moments were obtained at both of the specified Reynolds numbers. The streamwise flatness factor agrees with the HWA of Klewicki *et al.*[57] in the inner region, and the DNS of Schlatter & Örlü[58] throughout the boundary layer. A slight variation in the two sets of DNS profiles from BL_{6600} is observed between $Re_\theta = 4101$ and 5200. As mentioned in the Chapter 1, Reynolds number dependence of turbulent boundary layer statistics is considered by some groups to be a result of inappropriate scaling.[11] However, many groups have observed Reynolds number scaling for central moments in turbulent boundary layers similar to the differences in the BL_{6600} statistical profiles.[7,55,60,19,59] It has been argued that at very high Reynolds number statistics become asymptotic.[5] A small error in the calculation of the $Re_\theta = 4101$ statistics was discovered but the presented results are within a few percent of the true values for all comparisons with experiment data.

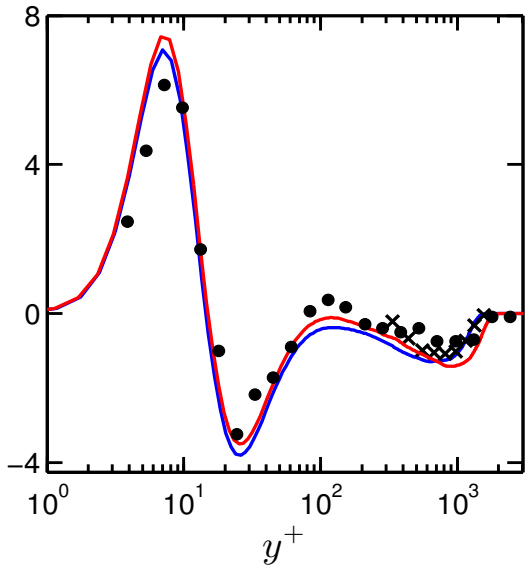

Figure 5.1: $\overline{u^3}^+$ inner scaling

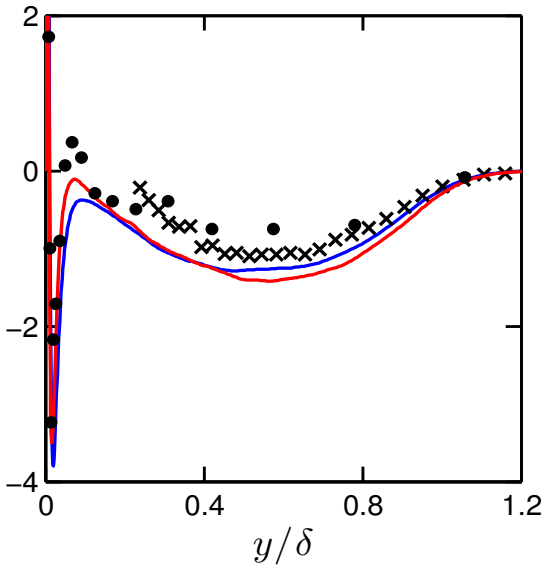

Figure 5.2: $\overline{u^3}^+$ outer scaling

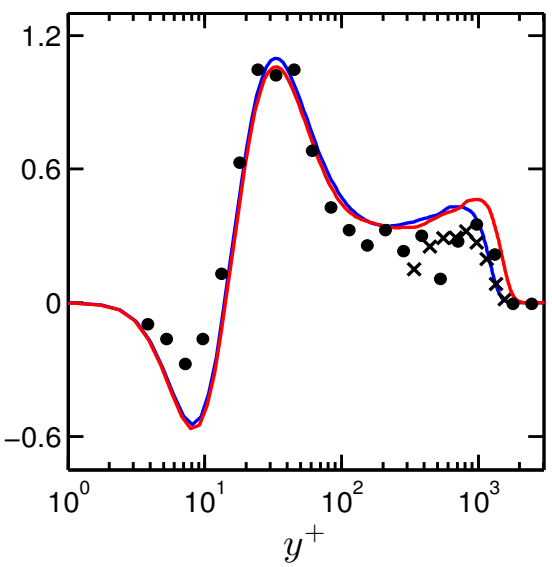

Figure 5.3: $\overline{u^2v}^+$ inner scaling

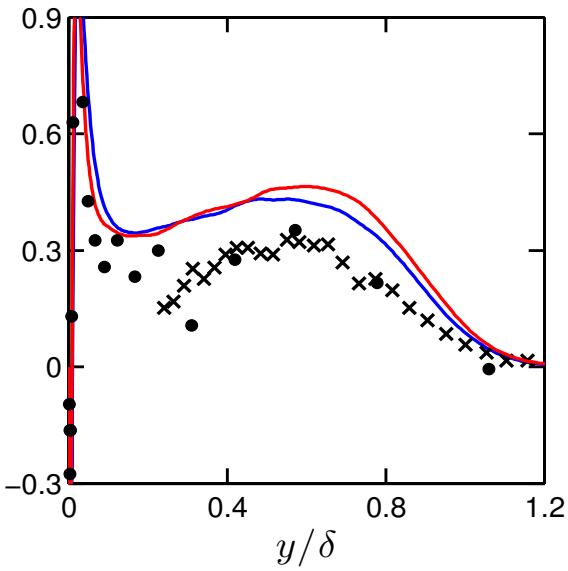

Figure 5.4: $\overline{u^2v}^+$ outer scaling

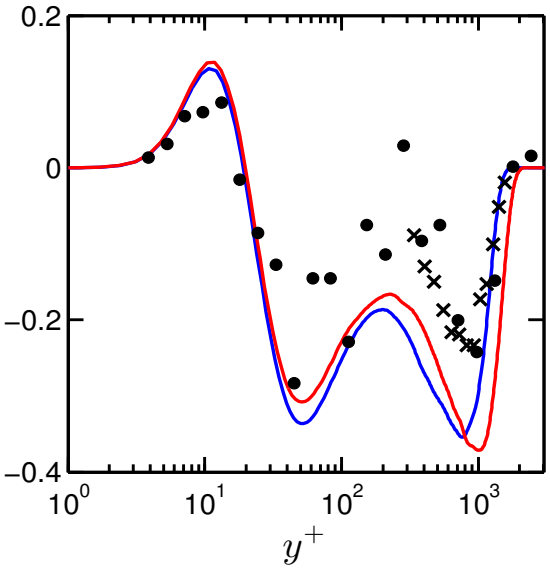

Figure 5.5: $\overline{uv^2}^+$ inner scaling

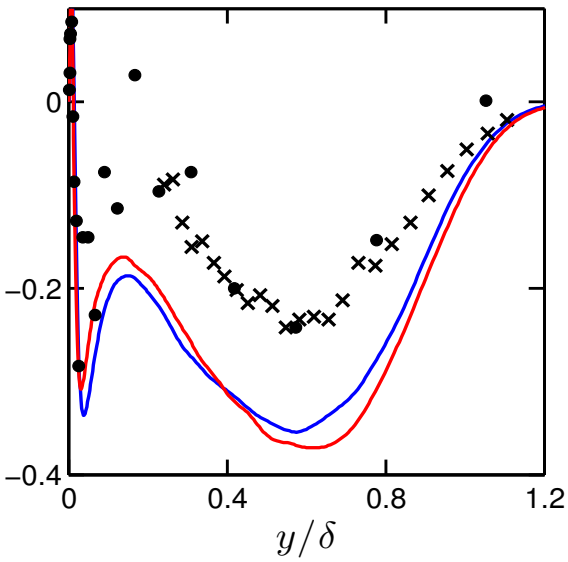

Figure 5.6: $\overline{uv^2}^+$ outer scaling

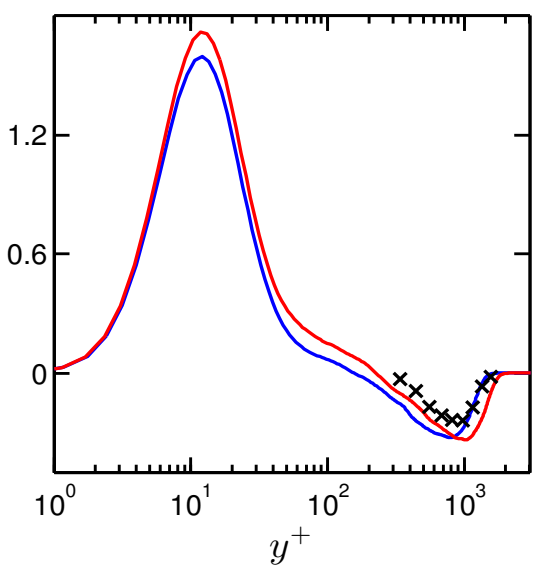

Figure 5.7: $\overline{uw^2}^+$ inner scaling

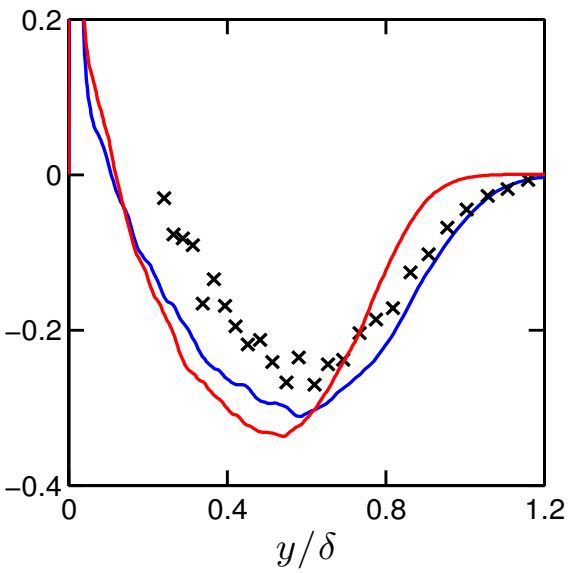

Figure 5.8: $\overline{uw^2}^+$ outer scaling

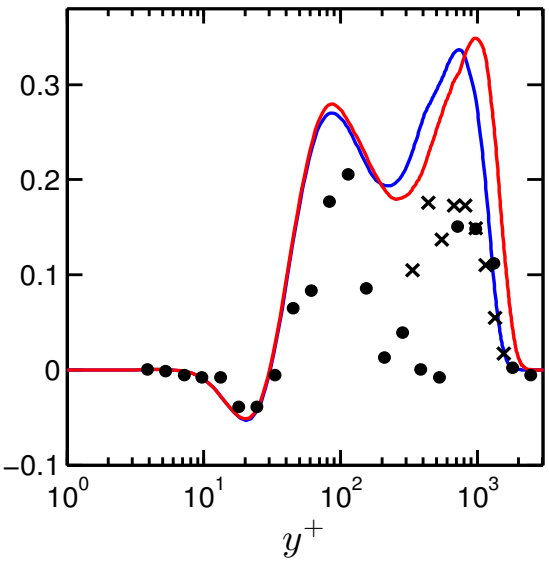

Figure 5.9: $\overline{v^3}^+$ inner scaling

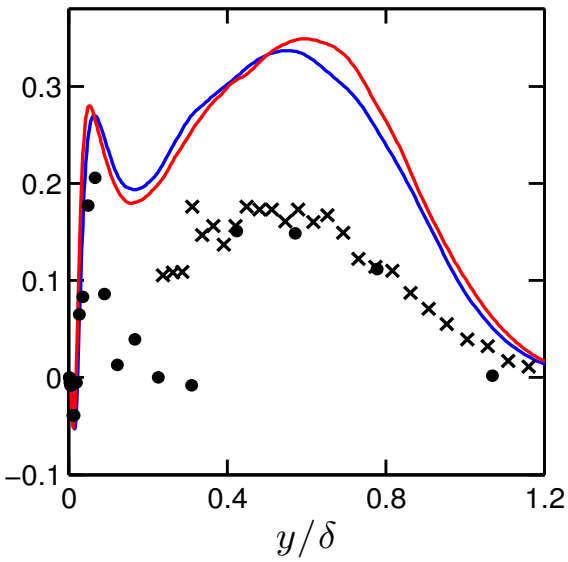

Figure 5.10: $\overline{v^3}^+$ outer scaling

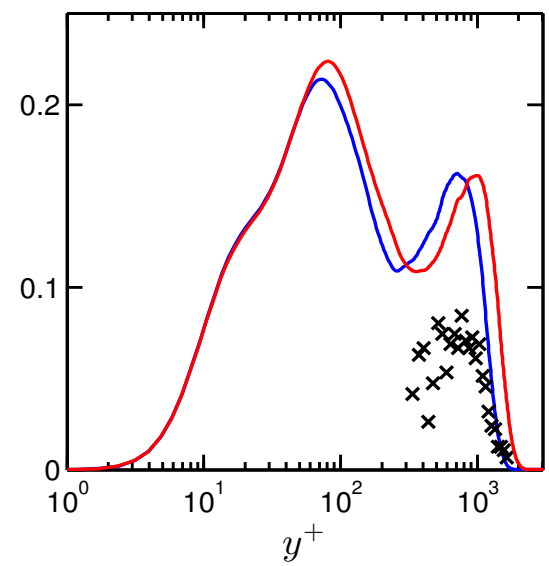

Figure 5.11: $\overline{vw^2}^+$ inner scaling

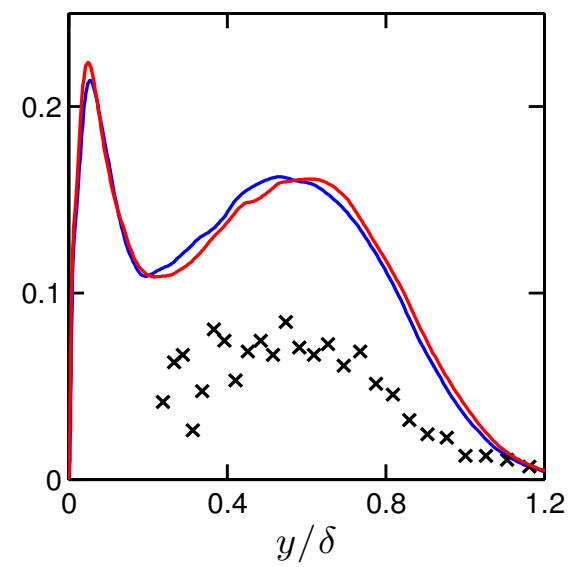

Figure 5.12: $\overline{vw^2}^+$ outer scaling

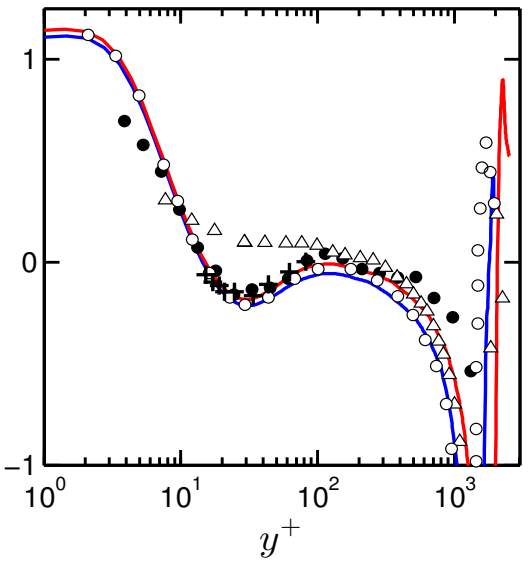

Figure 5.13: Streamwise skewness S_u

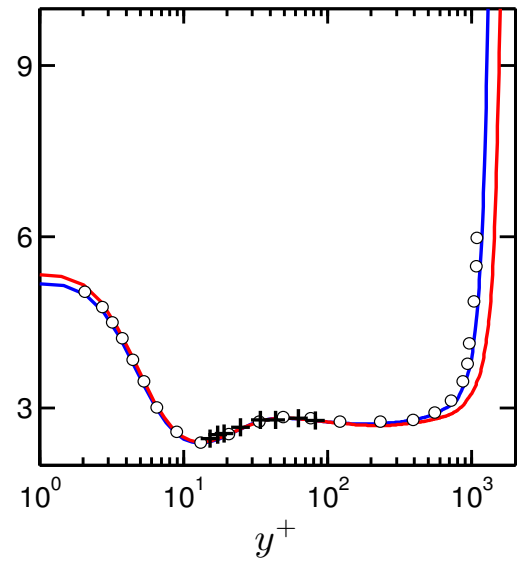

Figure 5.14: Streamwise flatness F_u

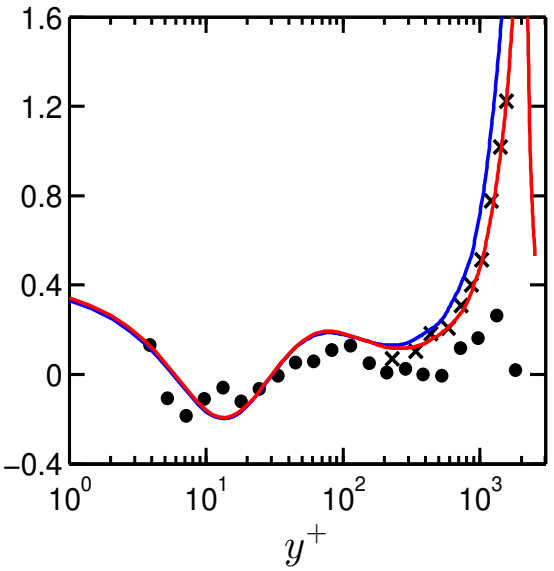

Figure 5.15: Wall-normal skewness S_v

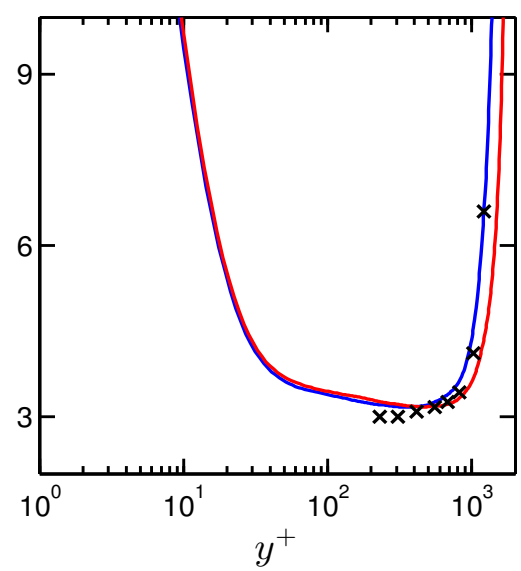

Figure 5.16: Wall-normal flatness F_v

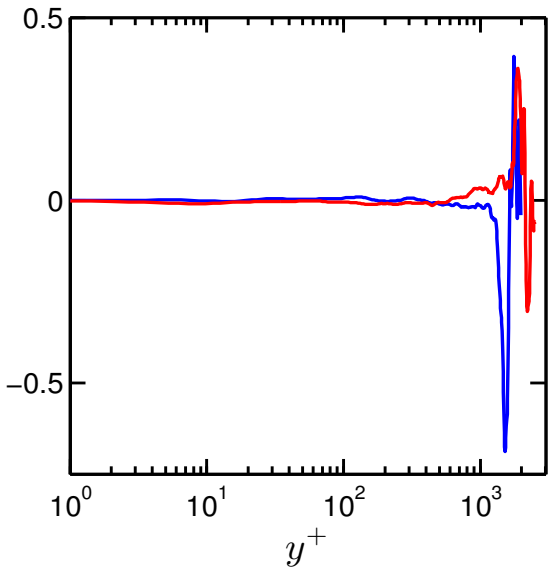

Figure 5.17: Spanwise skewness S_w

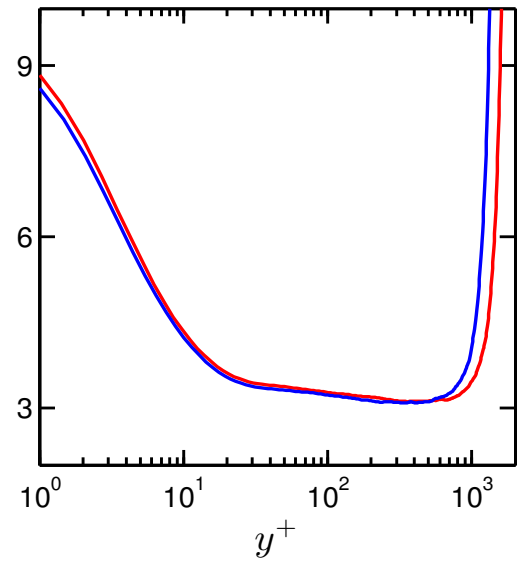

Figure 5.18: Spanwise flatness F_w

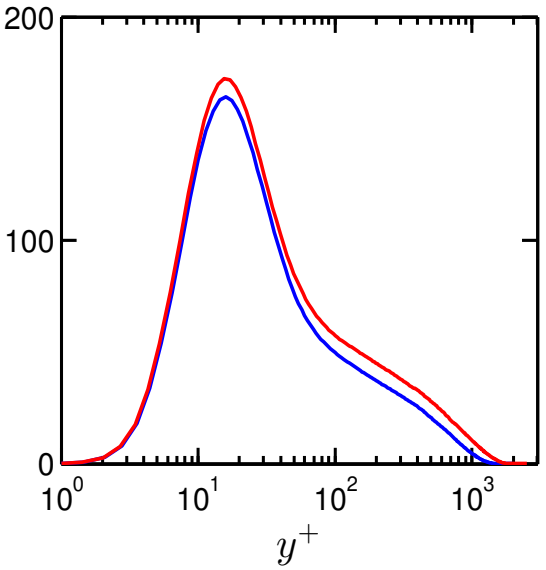

Figure 5.19: $\overline{u^4}^+$ inner scaling

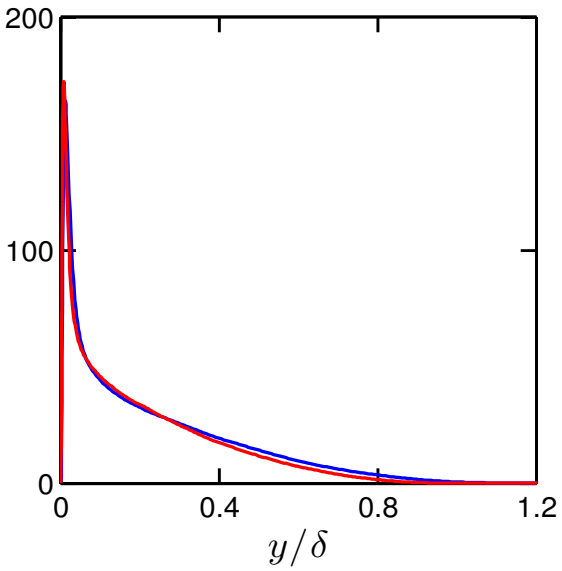

Figure 5.20: $\overline{u^4}^+$ outer scaling

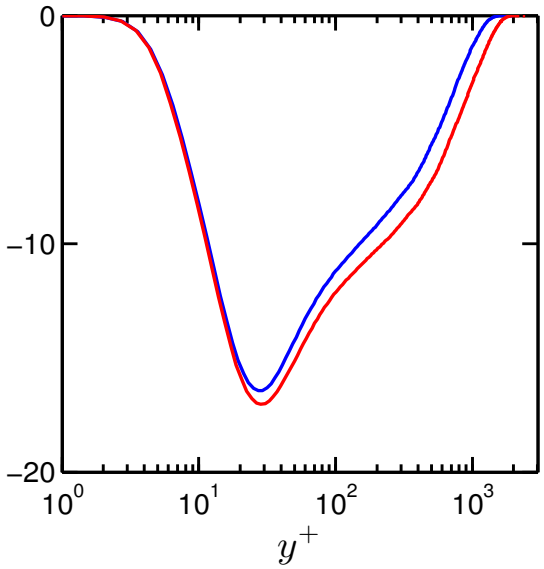

Figure 5.21: $\overline{u^3v}^+$ inner scaling

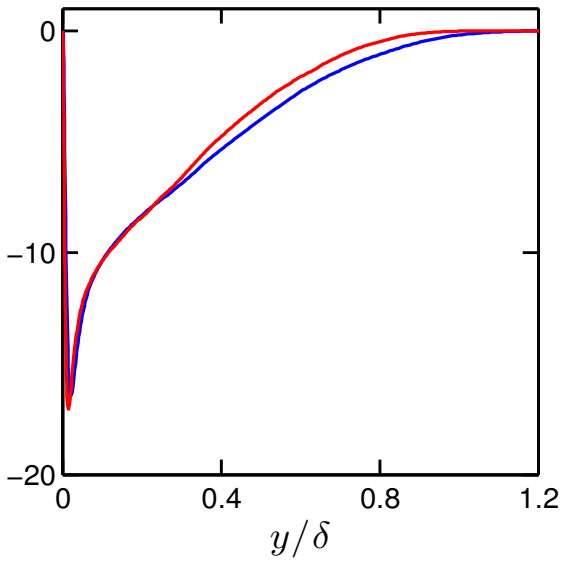

Figure 5.22: $\overline{u^3v}^+$ outer scaling

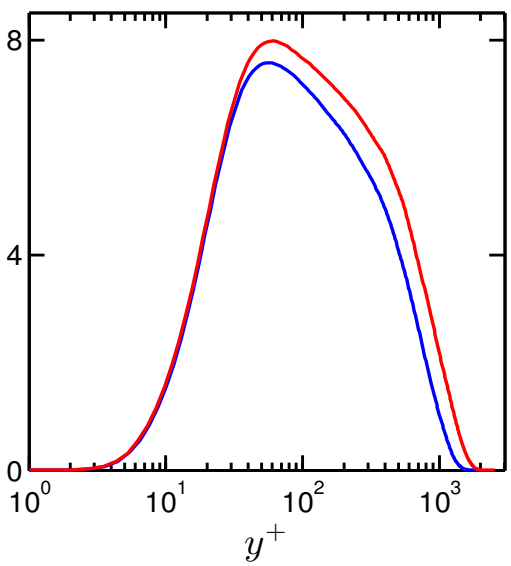

Figure 5.23: $\overline{u^2v^2}^+$ inner scaling

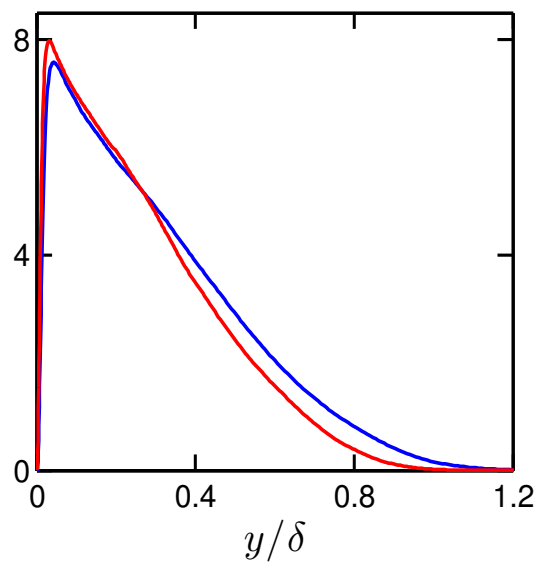

Figure 5.24: $\overline{u^2v^2}^+$ outer scaling

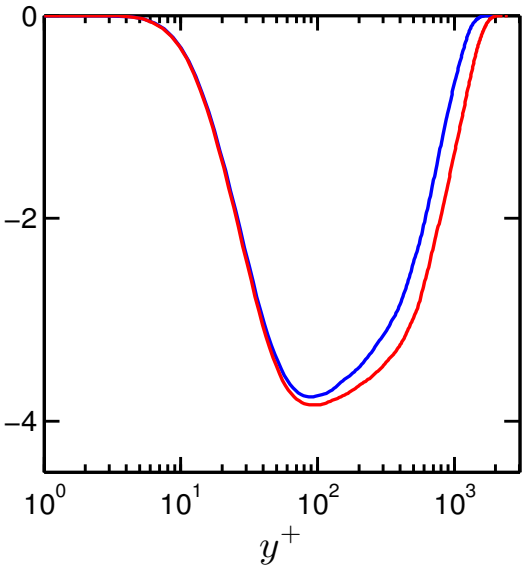

Figure 5.25: $\overline{uv^3}^+$ inner scaling

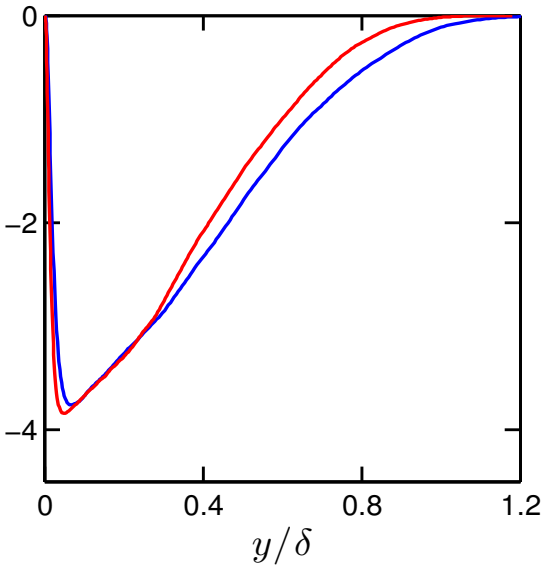

Figure 5.26: $\overline{uv^3}^+$ outer scaling

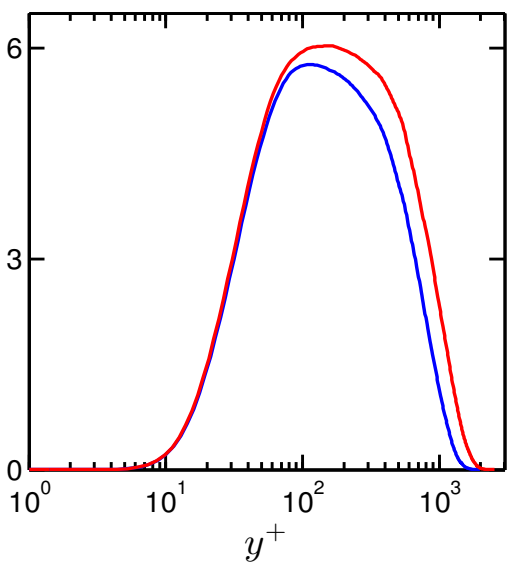

Figure 5.27: $\overline{v^4}^+$ inner scaling

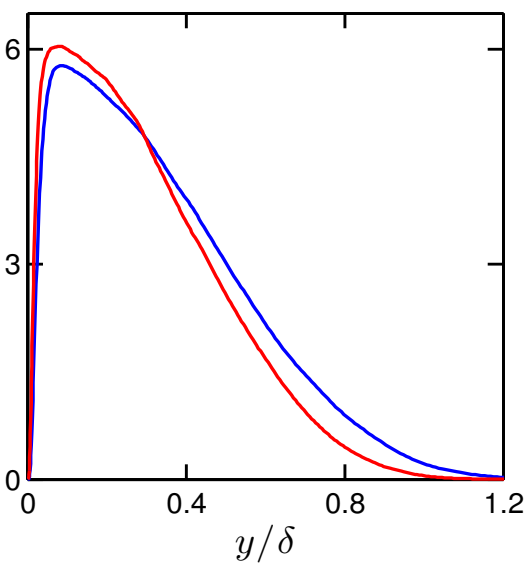

Figure 5.28: $\overline{v^4}^+$ outer scaling

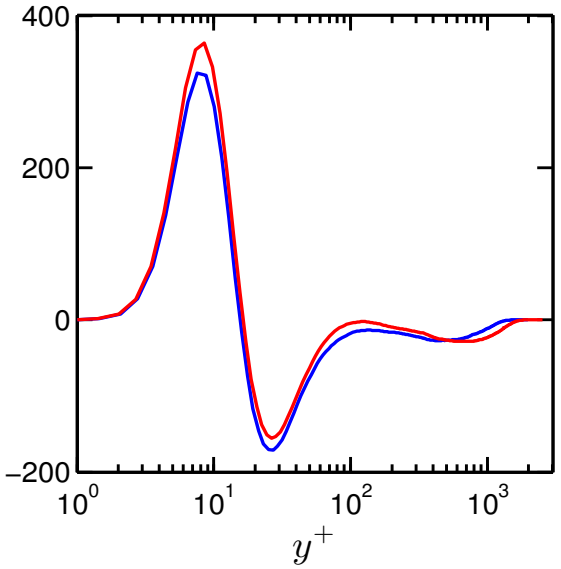

Figure 5.29: $\overline{u^5}^+$ inner scaling

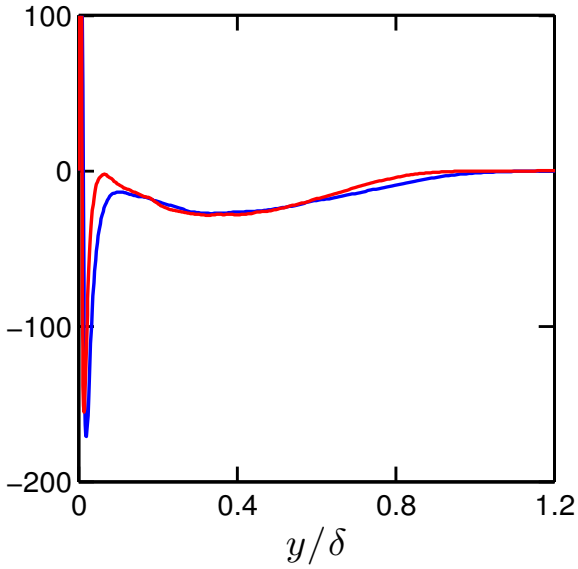

Figure 5.30: $\overline{u^5}^+$ outer scaling

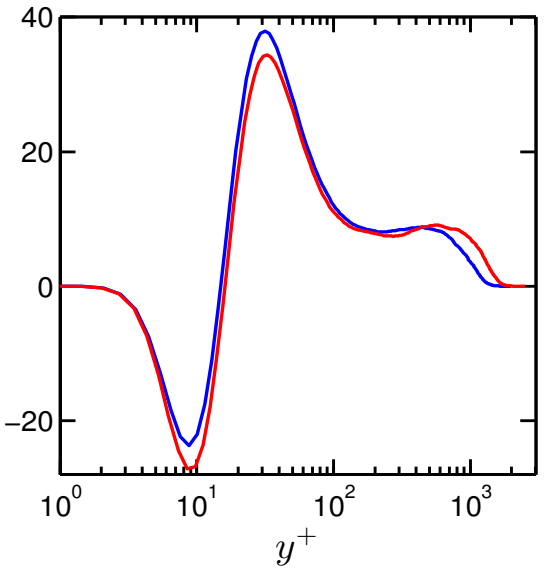

Figure 5.31: $\overline{u^4v}^+$ inner scaling

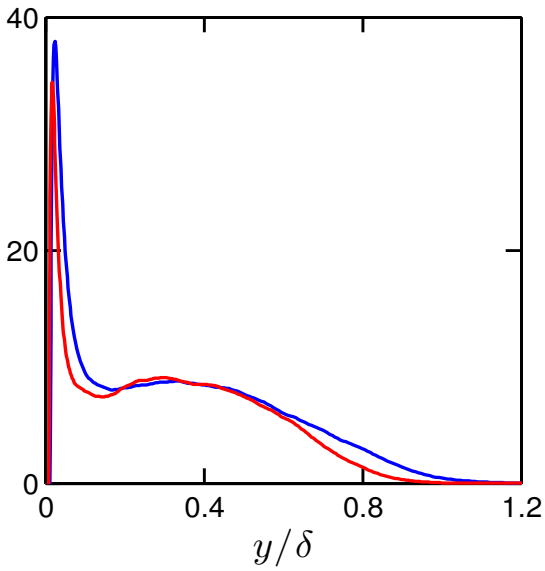

Figure 5.32: $\overline{u^4v}^+$ outer scaling

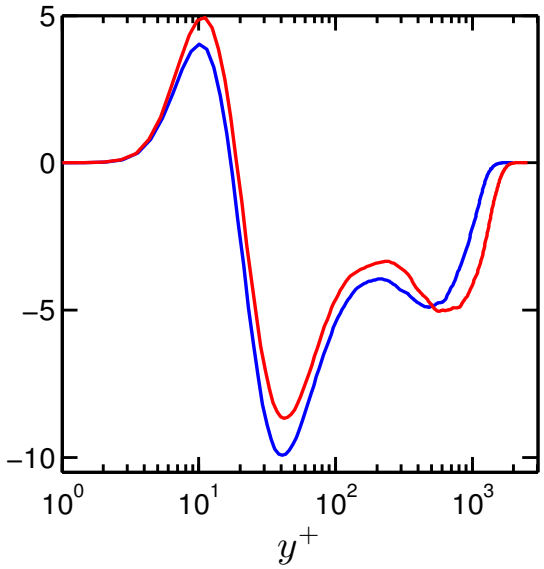

Figure 5.33: $\overline{u^3v^2}^+$ inner scaling

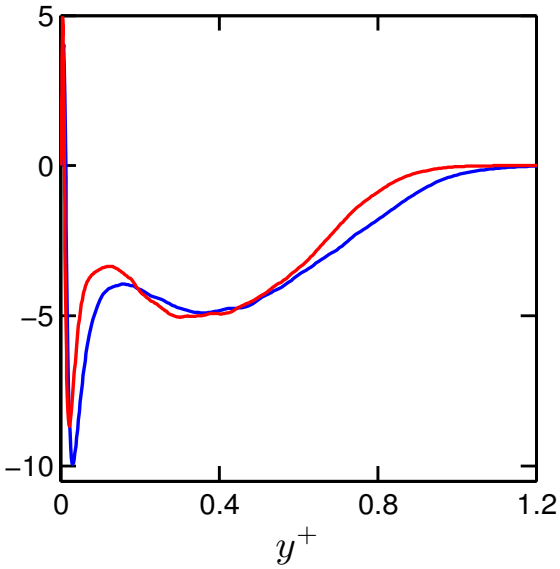

Figure 5.34: $\overline{u^3v^2}^+$ outer scaling

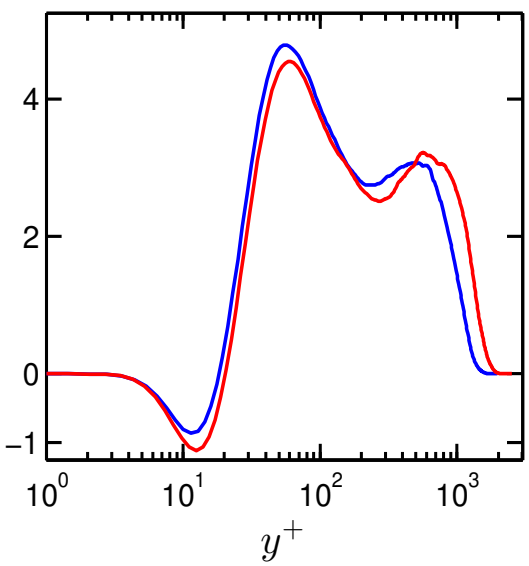

Figure 5.35: $\overline{u^2v^3}^+$ inner scaling

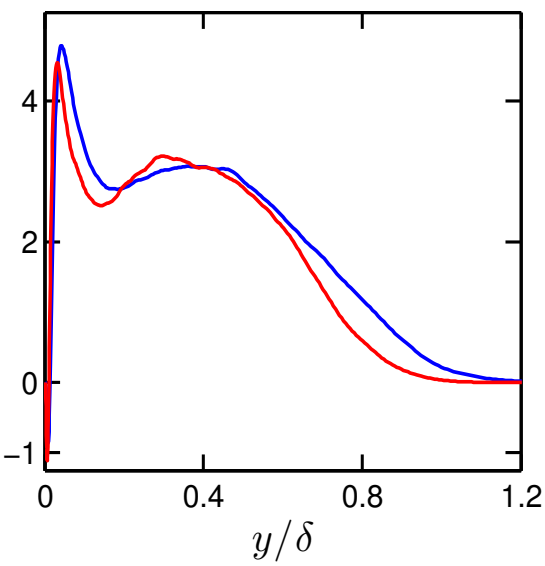

Figure 5.36: $\overline{u^2v^3}^+$ outer scaling

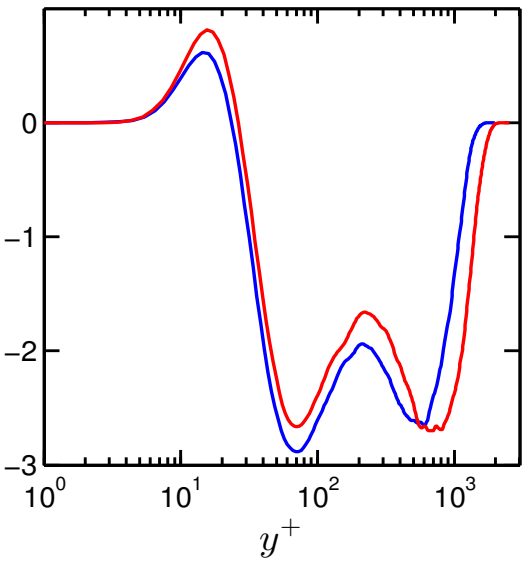

Figure 5.37: $\overline{uv^4}^+$ inner scaling

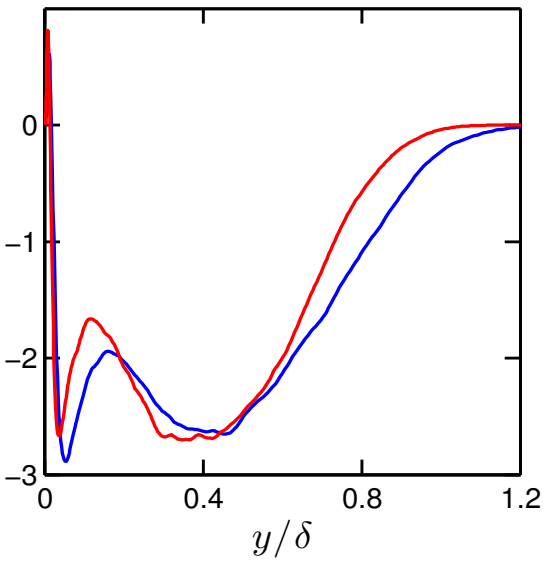

Figure 5.38: $\overline{uv^4}^+$ outer scaling

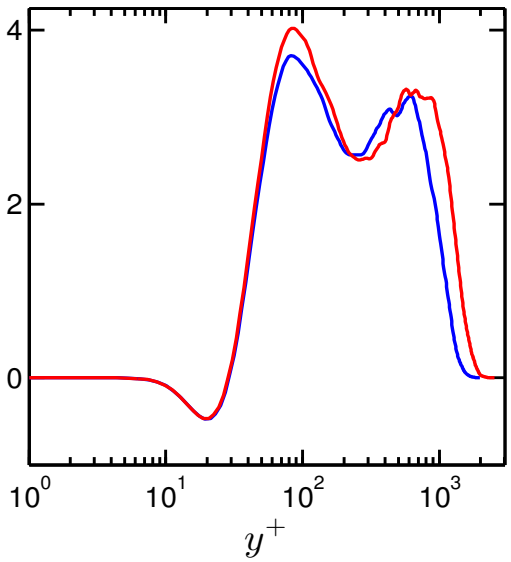

Figure 5.39: $\overline{v^5}^+$ inner scaling

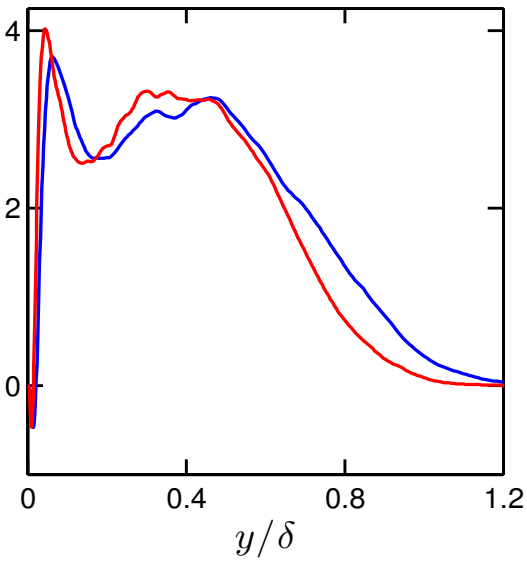

Figure 5.40: $\overline{v^5}^+$ outer scaling

5.2 Moment Interrelations from the Gram-Charlier series expansion procedure

Figures 5.41 to 5.60 show the interrelations of fifth-order moments constructed using the truncated Gram-Charlier series expansion procedure discussed in Section 4.2. The constructed moments are plotted as a dashed black line and solid black line for $Re_\theta = 4101$ and $Re_\theta = 5200$, respectively. As before, the blue lines correspond to BL_{6600} simulation data extracted at $Re_\theta = 4101$ and the red lines correspond to BL_{6600} simulation data extracted at $Re_\theta = 5200$.

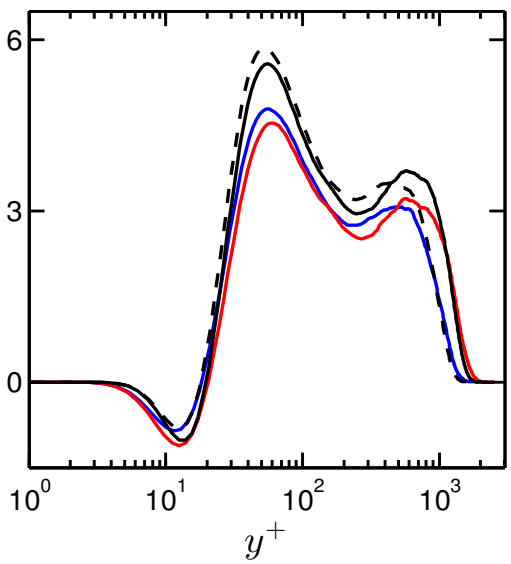

Figure 5.41: $\overline{u^2v^3}^+$ interrelation from the Gram-Charlier procedure, inner scaling

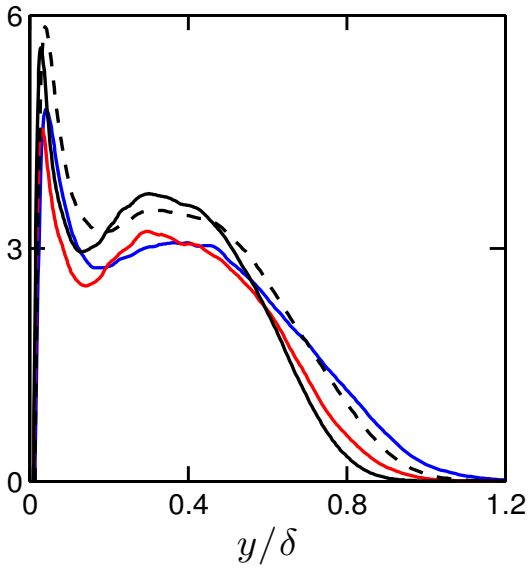

Figure 5.42: $\overline{u^2v^3}^+$ interrelation from the Gram-Charlier procedure, outer scaling

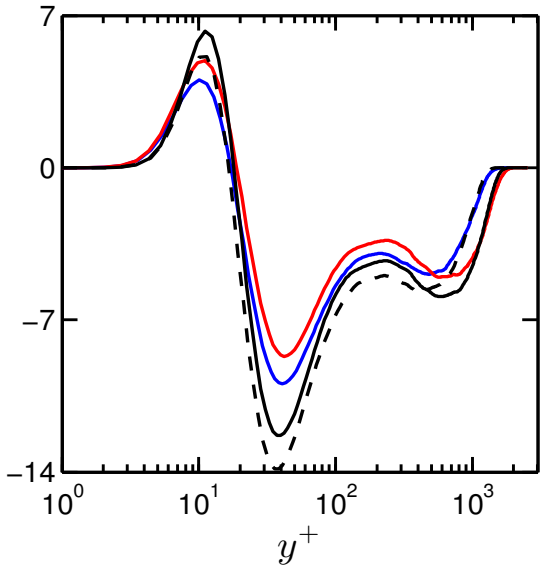

Figure 5.43: $\overline{u^3v^2}^+$ interrelation from the Gram-Charlier procedure, inner scaling

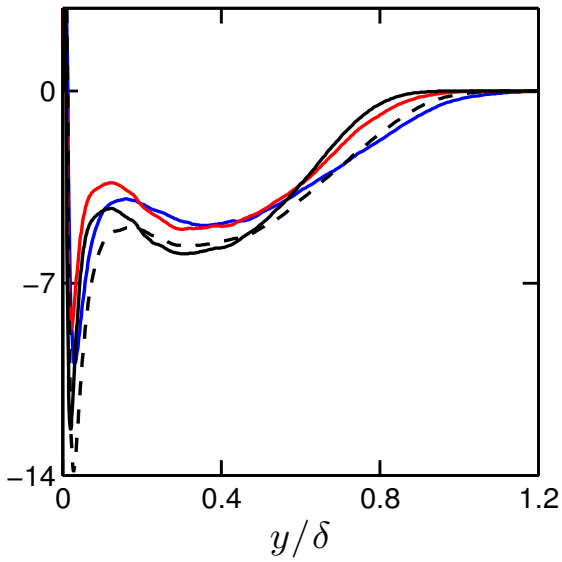

Figure 5.44: $\overline{u^3v^2}^+$ interrelation from the Gram-Charlier procedure, outer scaling

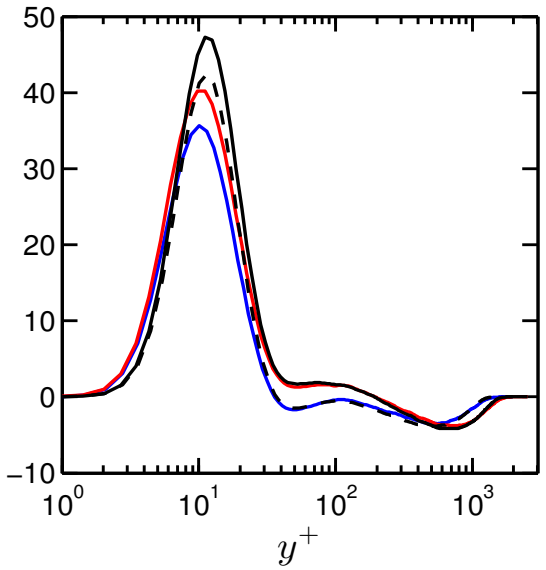

Figure 5.45: $\overline{u^3w^2}^+$ interrelation from the Gram-Charlier procedure, inner scaling

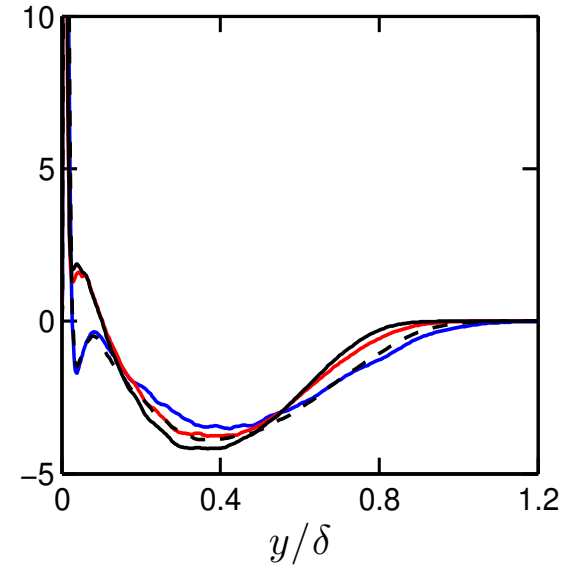

Figure 5.46: $\overline{u^3w^2}^+$ interrelation from the Gram-Charlier procedure, outer scaling

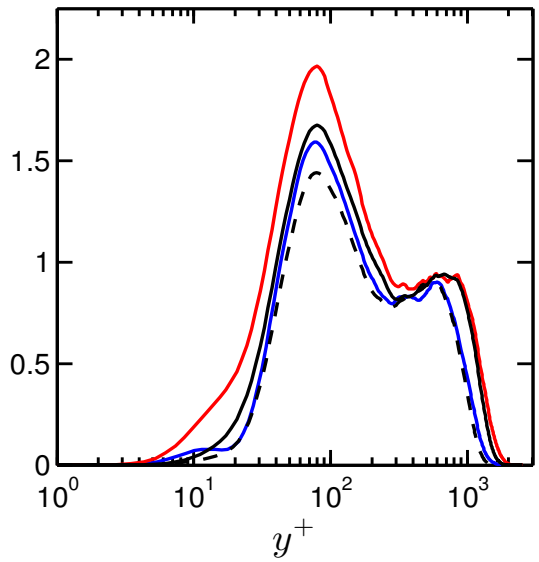

Figure 5.47: $\overline{v^3w^2}^+$ interrelation from the Gram-Charlier procedure, inner scaling

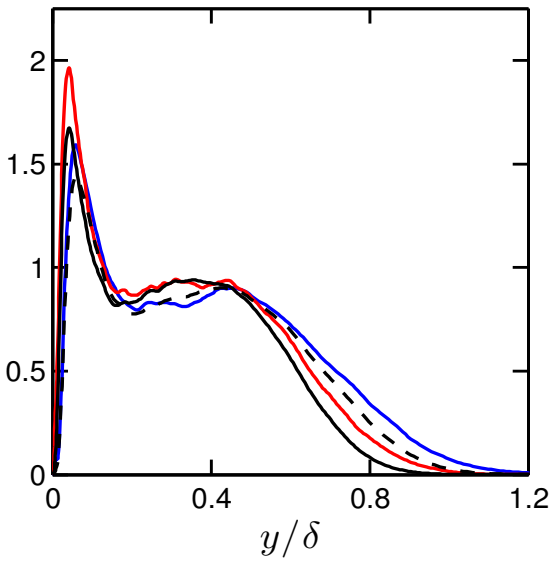

Figure 5.48: $\overline{v^3w^2}^+$ interrelation from the Gram-Charlier procedure, outer scaling

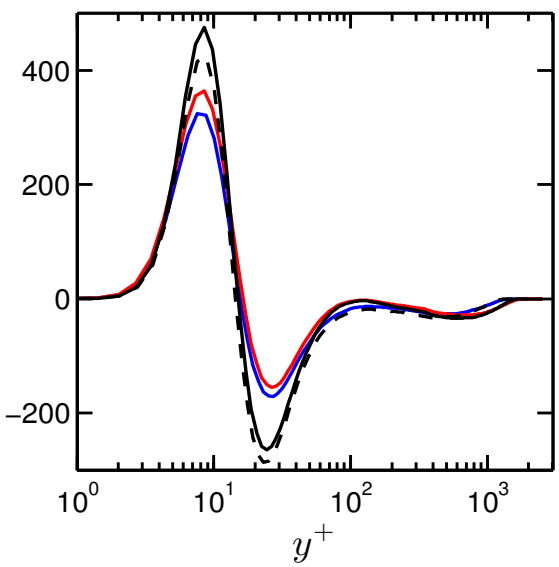

Figure 5.49: $\overline{u^5}^+$ interrelation from the Gram-Charlier procedure, inner scaling

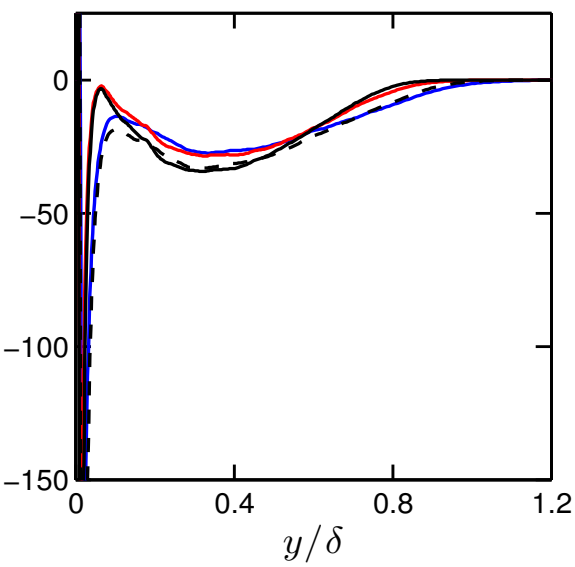

Figure 5.50: $\overline{u^5}^+$ interrelation from the Gram-Charlier procedure, outer scaling

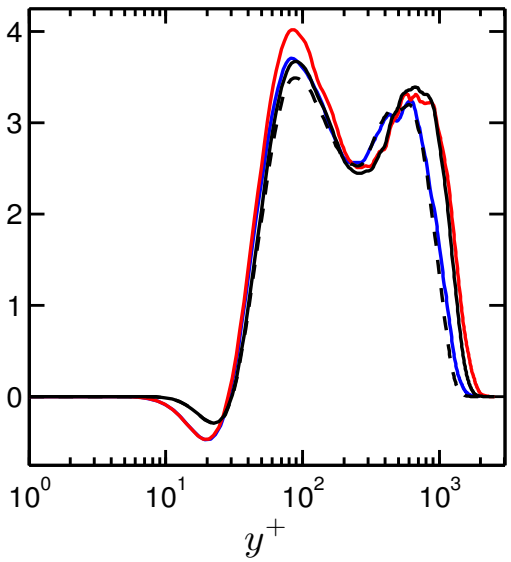

Figure 5.51: $\overline{v^5}^+$ interrelation from the Gram-Charlier procedure, inner scaling

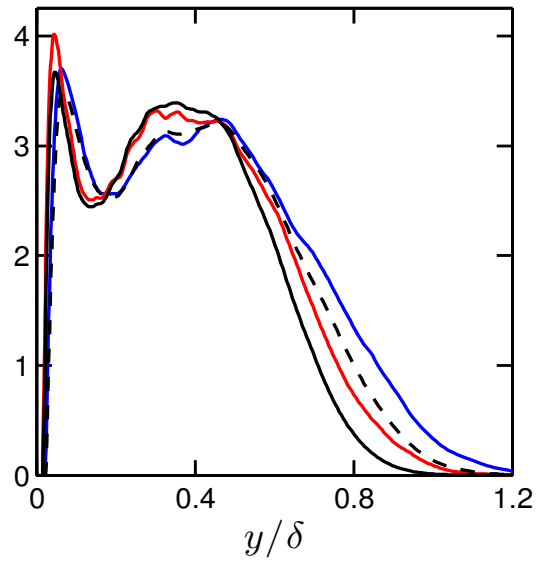

Figure 5.52: $\overline{v^5}^+$ interrelation from the Gram-Charlier procedure, outer scaling

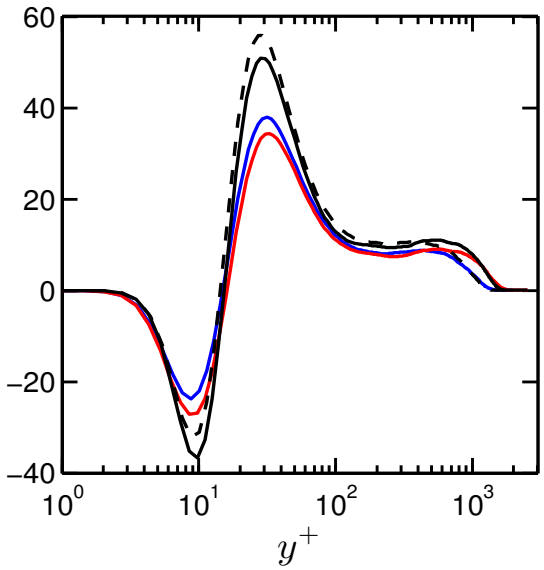

Figure 5.53: $\overline{u^4v}^+$ interrelation from the Gram-Charlier procedure, inner scaling

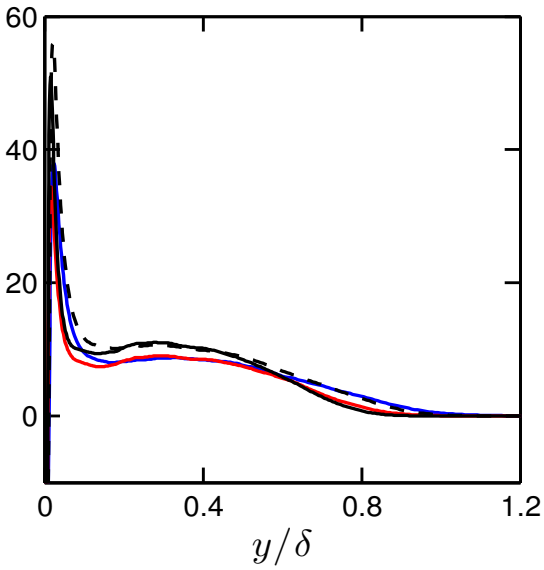

Figure 5.54: $\overline{u^4v}^+$ interrelation from the Gram-Charlier procedure, outer scaling

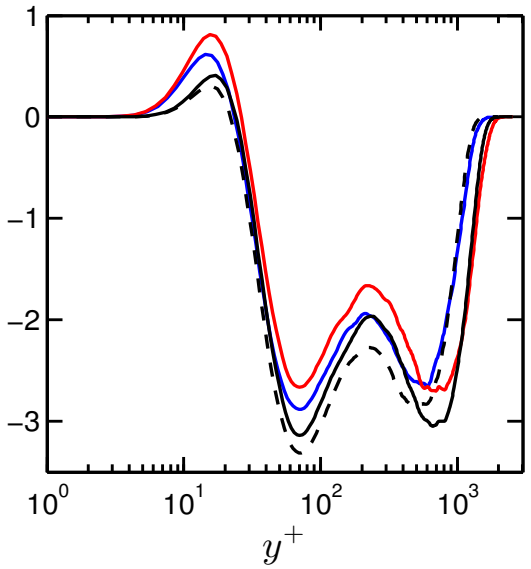

Figure 5.55: $\overline{uv^4}^+$ interrelation from the Gram-Charlier procedure, inner scaling

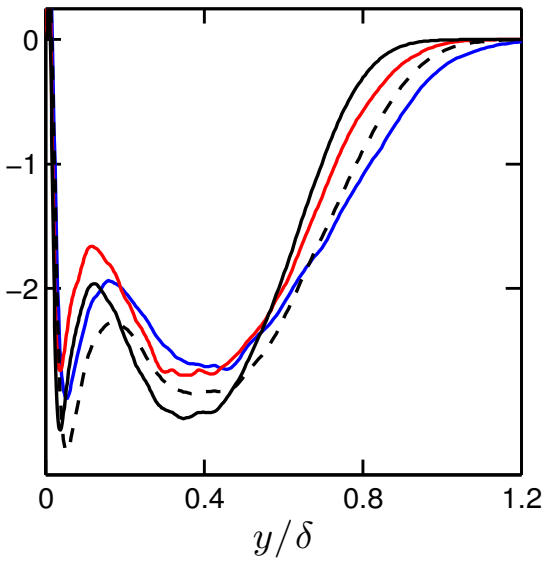

Figure 5.56: $\overline{uv^4}^+$ interrelation from the Gram-Charlier procedure, outer scaling

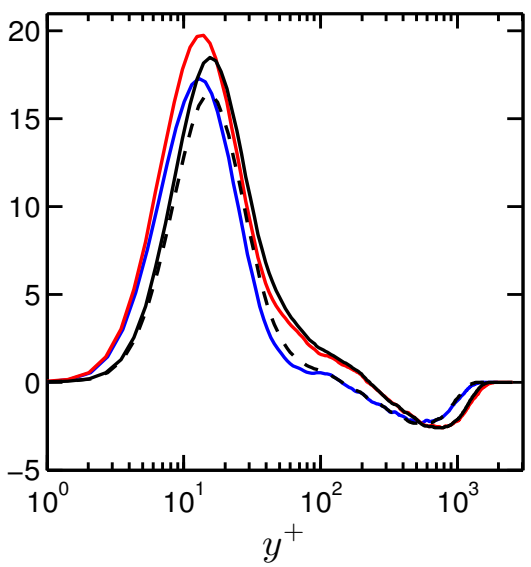

Figure 5.57: $\overline{uw^4}^+$ interrelation from the Gram-Charlier procedure, inner scaling

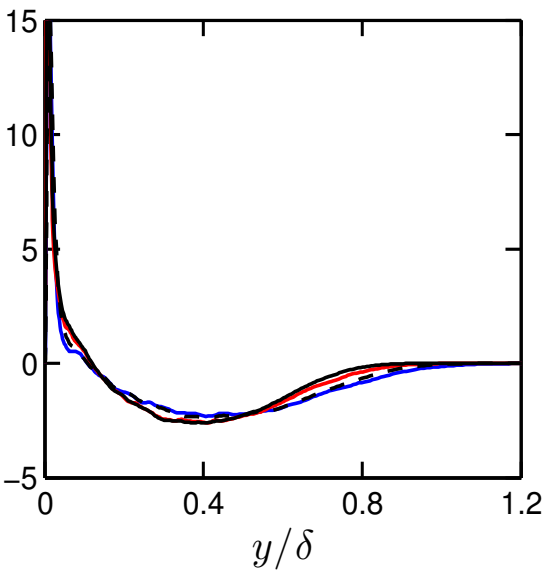

Figure 5.58: $\overline{uw^4}^+$ interrelation from the Gram-Charlier procedure, outer scaling

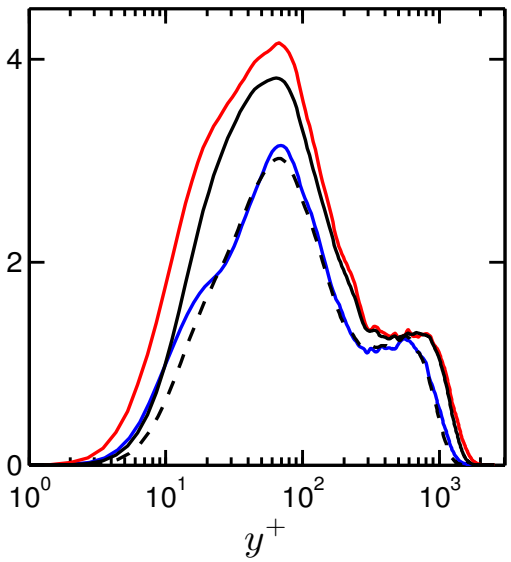

Figure 5.59: $\overline{vw^4}^+$ interrelation from the Gram-Charlier procedure, inner scaling

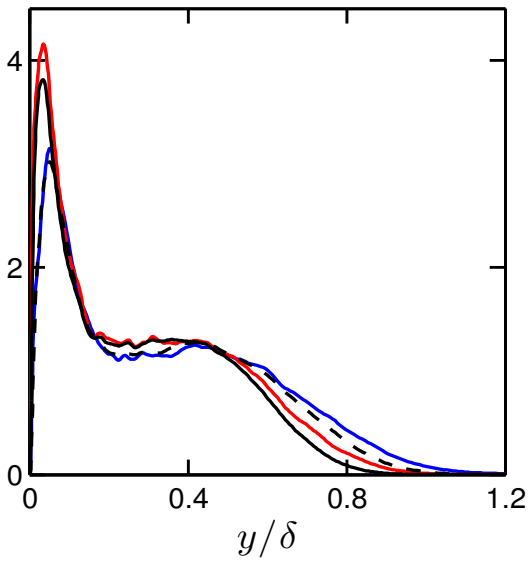

Figure 5.60: $\overline{vw^4}^+$ interrelation from the Gram-Charlier procedure, outer scaling

5.3 Moment Interrelations from Millionshtchikov's hypothesis

Figures 5.61 to 5.70 show the fourth-order moment interrelations constructed using the Millionshtchikov quasinormality hypothesis procedure discussed in Section 4.2. The figures demonstrate that the assumption of a Gaussian turbulent velocity field[10] is rather weak in the considered flow; it is a reasonable approximation for $\overline{uv^3}$ and $\overline{u^2v^2}$, but gives only qualitative agreement for $\overline{u^3v}$. As before, the constructed moments are plotted as a dashed black line and solid black line for $Re_\theta = 4101$ and $Re_\theta = 5200$, respectively. The blue lines correspond to BL_{6600} simulation data extracted at $Re_\theta = 4101$ and the red lines correspond to BL_{6600} simulation data extracted at $Re_\theta = 5200$.

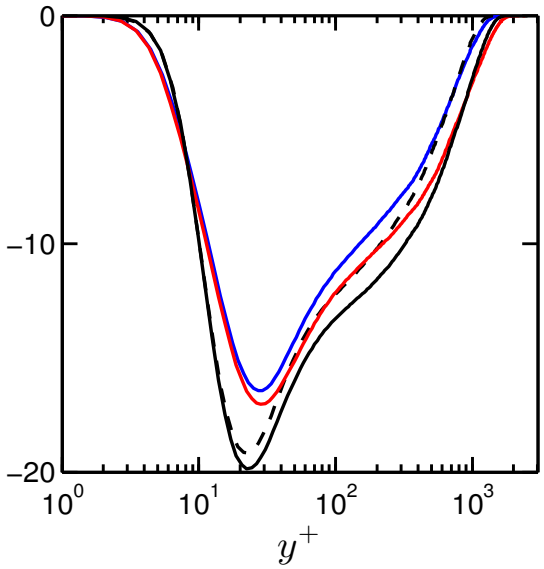

Figure 5.61: $\overline{u^3v}^+$ interrelation from the quasinormality procedure, inner scaling

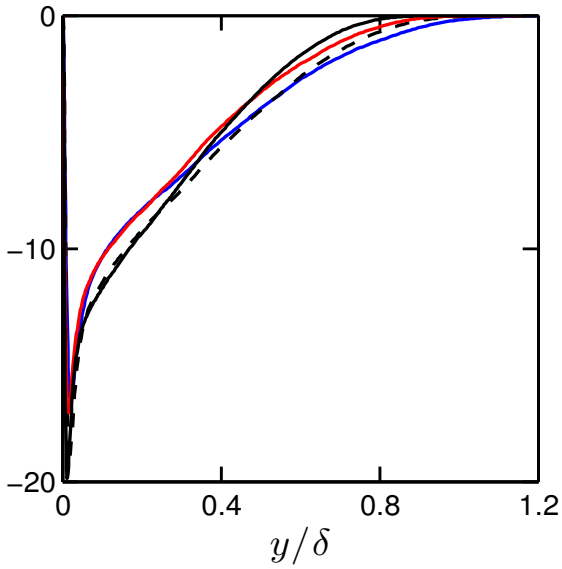

Figure 5.62: $\overline{u^3v}^+$ interrelation from the quasinormality procedure, outer scaling

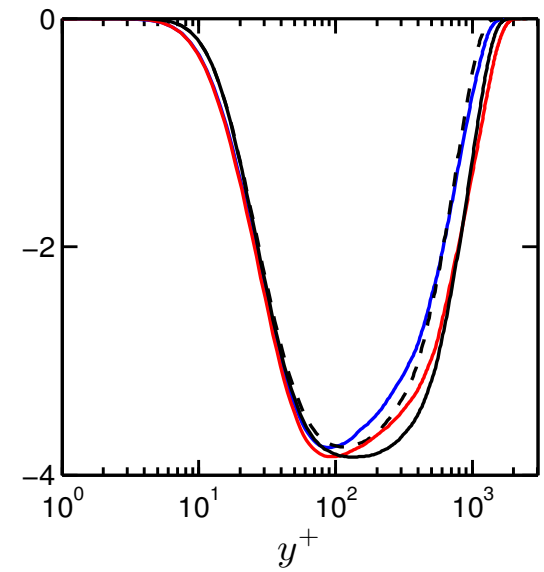

Figure 5.63: $\overline{uv^3}^+$ interrelation from the quasinormality procedure, inner scaling

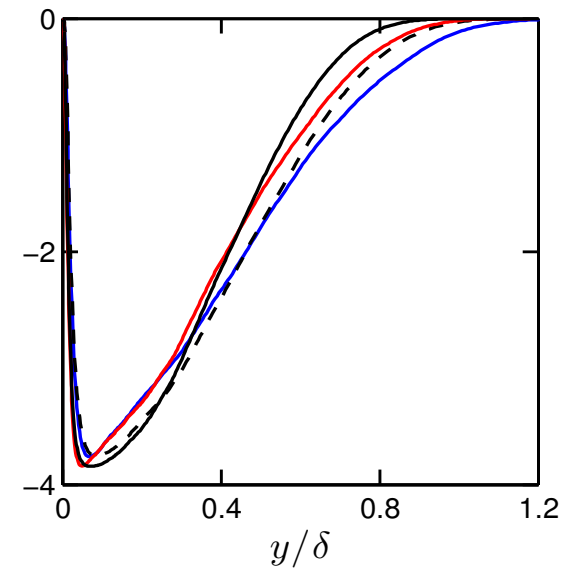

Figure 5.64: $\overline{uv^3}^+$ interrelation from the quasinormality procedure, outer scaling

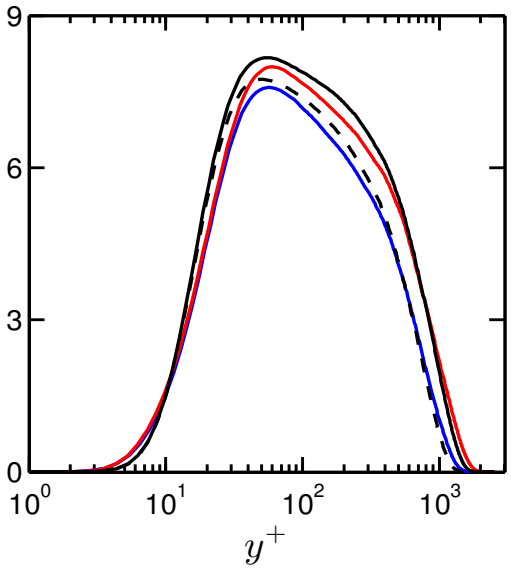

Figure 5.65: $\overline{u^2v^2}^+$ interrelation from the quasinormality procedure, inner scaling

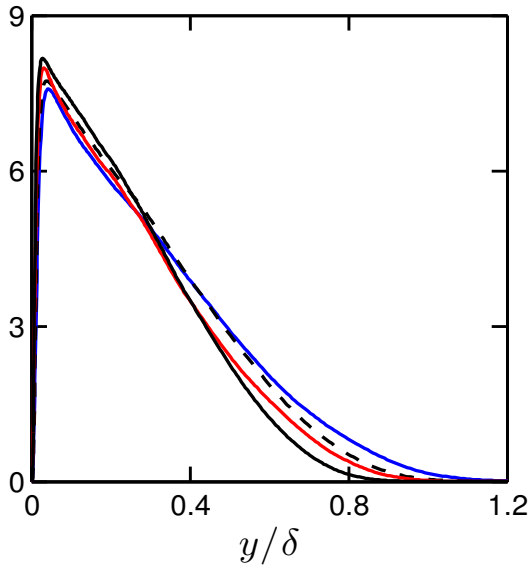

Figure 5.66: $\overline{u^2v^2}^+$ interrelation from the quasinormality procedure, outer scaling

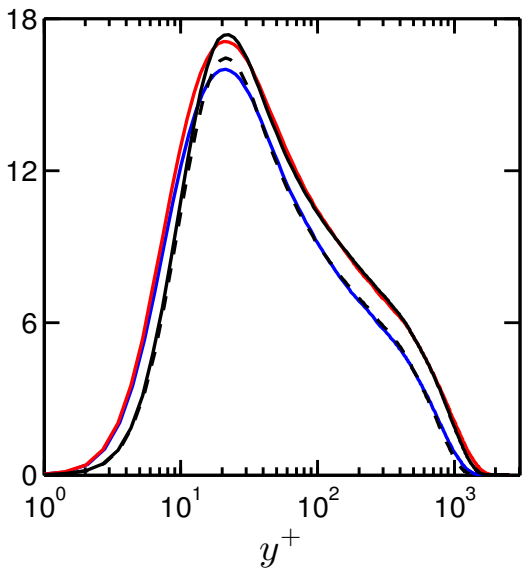

Figure 5.67: $\overline{u^2w^2}^+$ interrelation from the quasinormality procedure, inner scaling

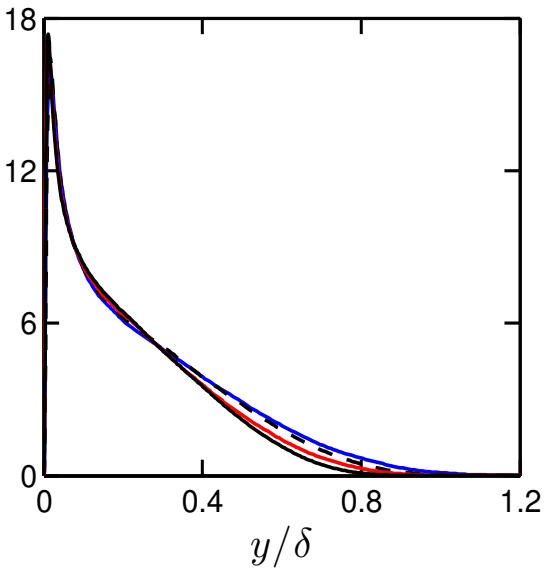

Figure 5.68: $\overline{u^2w^2}^+$ interrelation from the quasinormality procedure, outer scaling

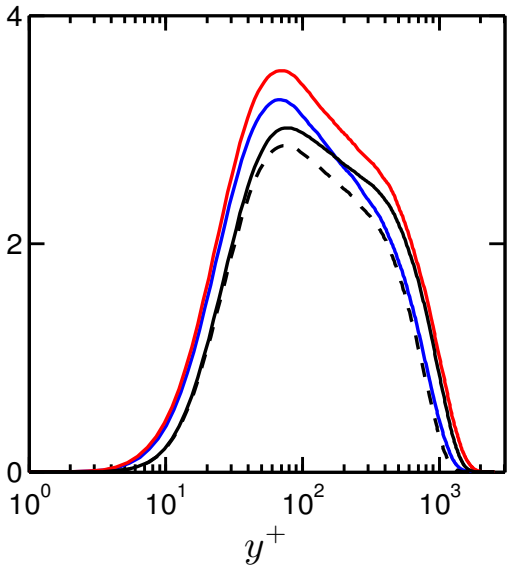

Figure 5.69: $\overline{v^2w^2}^+$ interrelation from the quasinormality procedure, inner scaling

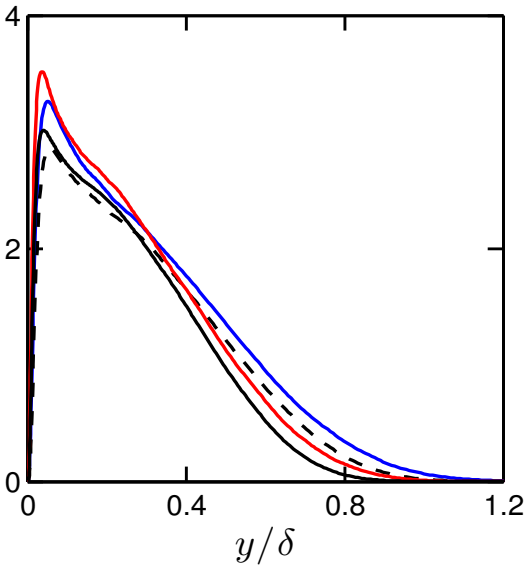

Figure 5.70: $\overline{v^2w^2}^+$ interrelation from the quasinormality procedure, outer scaling

5.4 Visualization of Turbulent Structures

Near the wall in a turbulent boundary layer, alternating streaks of high- and low-speed fluid in the viscous and buffer layers extend in the streamwise direction. Near wall streaks are $x^+ = 200$ - 1000 in length and $z^+ = 100$ in width on average, where x^+,y^+, and z^+, are streamwise, wall-normal, and spanwise coordinates normalized by u_τ/ν, respectively.[17,61,62,63] It has been observed that the low-speed streaks rise from the wall and oscillate in $8 < y^+ < 12$, followed by an abrupt disintegration of the fluid pocket in the buffer layer around $10 < y^+ < 30$.[62] The process is called bursting and is considered to be intermittent, quasi-cyclic, and the primary mechanism for the production of turbulent kinetic energy.[1,4] The bursting phenomenon has been linked to quasi-streamwise vortical activity.[64]

Another observed turbulent structure that occurs in the viscous and buffer lay-

ers is referred to as a localized shear layer.[65,66,67,68,69] Localized shear layers occur between pockets of fluid with drastically different velocities and are thought to originate from low-speed fluid moving away from the wall, also known as an ejection.[4] Ejections are associated with a sharp drop in $\partial\omega_z/\partial y$, where ω_z is the spanwise curl of the velocity field,[70] and may extend from the buffer layer into the log layer.[62] As low-speed fluid moves away from the wall, high-speed fluid rushes down into the viscous sublayer in an event known as a sweep.[67,62] Opposite to an ejection, sweeps are associated with a sharp rise in $\partial\omega_z/\partial y$.[62]

The large eddy structures in the wake region have been observed to contain structures that are elongated in the streamwise direction[66] and characterized by transverse velocities.[71] It has been observed that large scale intermittency is found in external turbulent boundary layers but not in internal turbulent boundary layers.[8]

Several researchers have found evidence of low-speed streaks, bursting motions, and localized shear layers in experiments and suggested that observed phenomena result from the dynamics of vortex loops inclined at roughly 45 degrees above the wall, called hairpin vortices.[72,73,74,14,59] A smoke visualization by Head & Bandyopadhyay[75] directly observed hairpin vortices extending to the outer edge of the boundary layer. The relatively large turbulence trips used in their experiment, however, have led others to speculate that the hairpins they observed did not evolve due to flow instabilities and therefore the experiment is not representative of the canonical turbulent boundary layer.[76] In addition, Head & Bandyopadhyay[75] report that for $Re_\theta > 5000$ the vortex pairs or hairpins become so stretched that the name hairpin vortex ceases to describe the structure. Erm & Joubert[77] performed turbulent boundary layer measurements using three different trip mechanisms and concluded that the effects of a turbulence trip are negligible only for $Re_\theta > 1500$. It is conceivable that the larger the turbulence trip relative to the flow parameters, the longer the streamwise distance affected by the trip, and so it seems plausible that

the hairpin vortices observed by Head & Bandyopadhyay[75] are an artifact of their turbulence trip. Bernard & Wallace[4], Bernard *et al.*,[78] and Robinson[1] agree that a vortical description of turbulence production mechanisms in the boundary layer is the most useful description, and they postulate that half-horsehoe or half-hairpin quasi-streamwise vortices are the most common vortical structures in the turbulent boundary layer.

Unlike vorticity, a vortex has no precise mathematical definition. In a turbulent boundary layer, regions of strong vorticity do not necessarily correspond to the presence of vortices.[1] Robinson *et al.*[1] proposed a qualitative definition of a vortex: "A vortex exists when instantaneous streamlines mapped onto a plane normal to the vortex core exhibit a roughly circular or spiral pattern when viewed from a reference frame moving with the center of the vortex core." In experiments, it is difficult to outline vortical structures,[4] and objective vortex detection methods for DNS are a topic of ongoing research.[79,4,80]

The Q critierion was selected as the vortex detection method for this study to directly compare the flow field of the BL_{6600} simulation with the flow field published by Wu & Moin[76] that visualizes hairpin vortices. The Q criterion is formulated in terms of the second invariant of the velocity gradient tensor for incompressible flow in Equation (5.1).[81]

$$Q = \frac{1}{2}(||\Omega||^2 - ||S||^2). \tag{5.1}$$

Here $||A||$ is the Euclidean (or Frobenius) matrix norm of A. Coherent vortices are defined as the region where $Q > 0$, where the rate of clockwise rotation of an infinitesimal fluid element about its centroid is greater than the rate of shearing action acting on the infinitesimal fluid element.[81] The isosurfaces of Figures 5.71 to 5.76 show the isosurfaces of $Q = 0$ colored by normalized local total velocities.

Observed low-speed ejections at $Re_\theta = 5200$ in Figures 5.71-5.74 extend from

the buffer layer into the log layer in agreement with the measurements of Honkan & Andreopoulos[70] are shown in detail in Figures 5.75 and 5.76. Figures 5.75 and 5.76 also show quasi-streamwise vortical structures in the buffer and log layers that appear to disintegrate as they rise, in agreement with the concept of the bursting process.[64,1,4] The lowest reaches of the high-speed sweeps stop short of extending into the viscous sublayer, in disagreement with previous experimental observations.[62,4] The blue colored near-wall streaks are apparent in Figures 5.75-5.76, and their streamwise dimension, $x^+ = 200$ - 1000 corresponds to those for similar Reynolds numbers observed by Gupta *et al.*[63] and for lower Reynolds numbers observed by Kline *et al.*[62] However, their spanwise width is approximately $x^+ = 40$, much narrower than observations. The presence of localized shear layers is suggested in Figures 5.71-5.73 by steep gradients in the isosurface color.

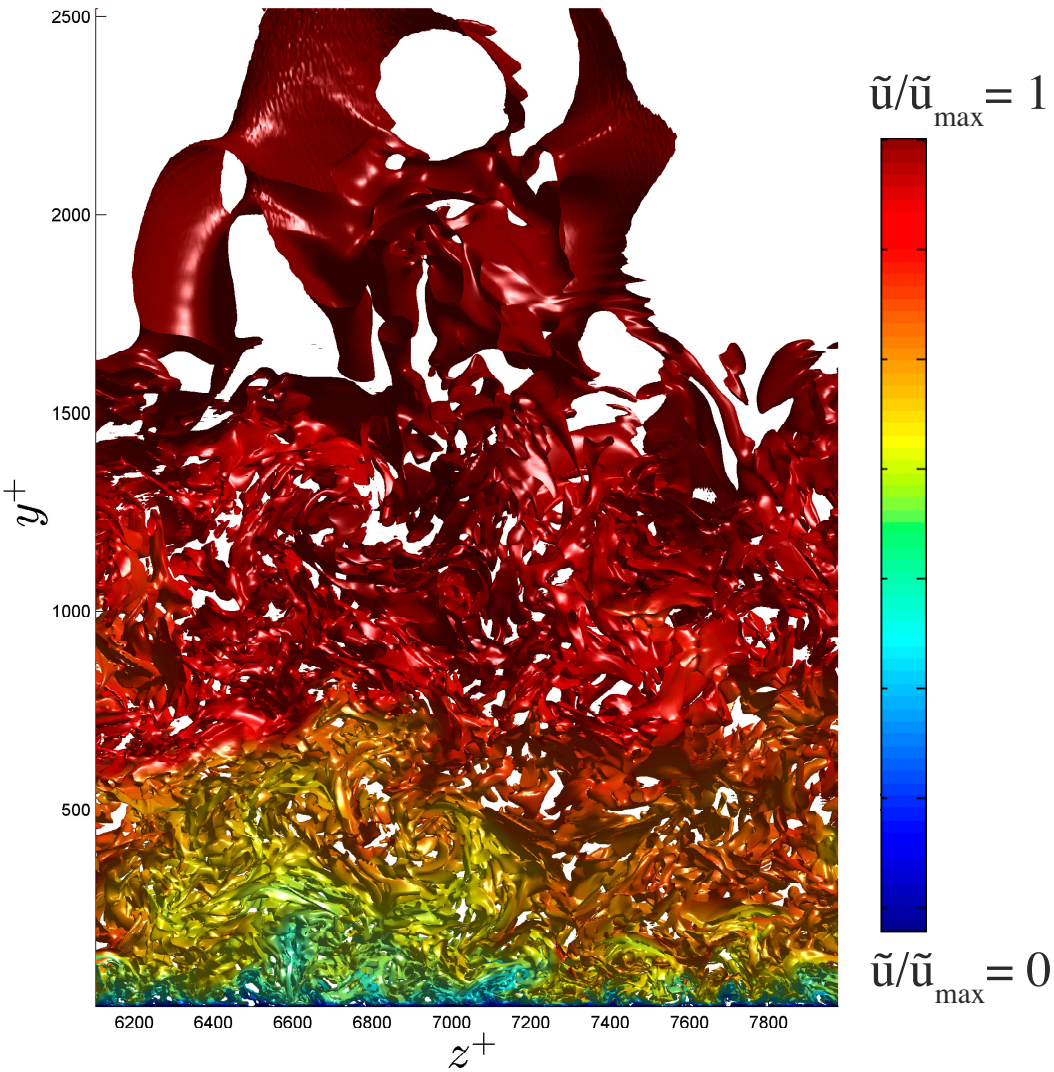

Figure 5.71: Streamwise view of the Q criterion isosurface colored by total streamwise velocity $\tilde{u}$ at $Re_\theta = 5200$

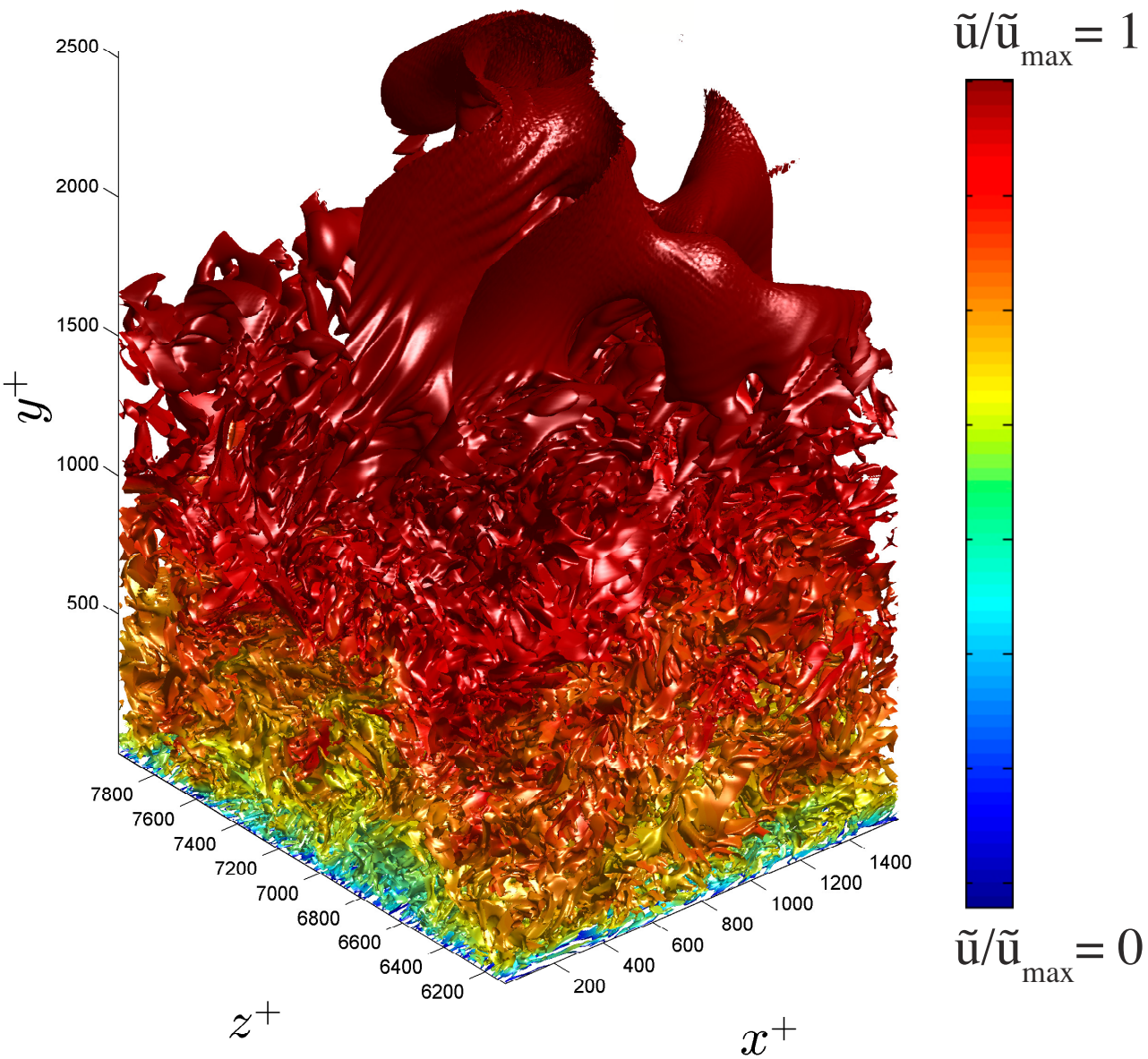

Figure 5.72: Isometric view of the Q criterion isosurface colored by total streamwise velocity $\tilde{u}$ at $Re_\theta = 5200$

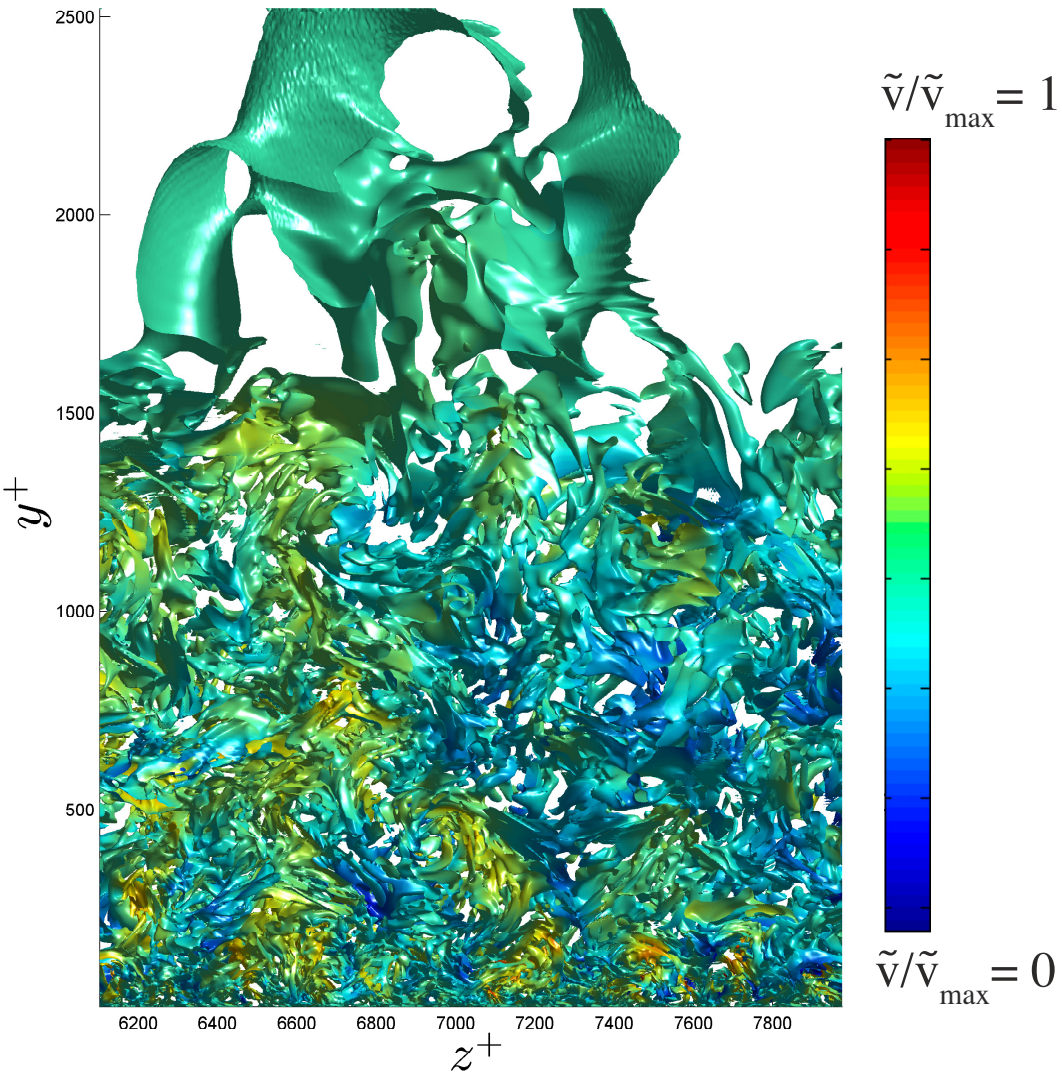

Figure 5.73: Streamwise view of the Q criterion isosurface colored by total wall-normal velocity $\tilde{v}$ at $Re_\theta = 5200$

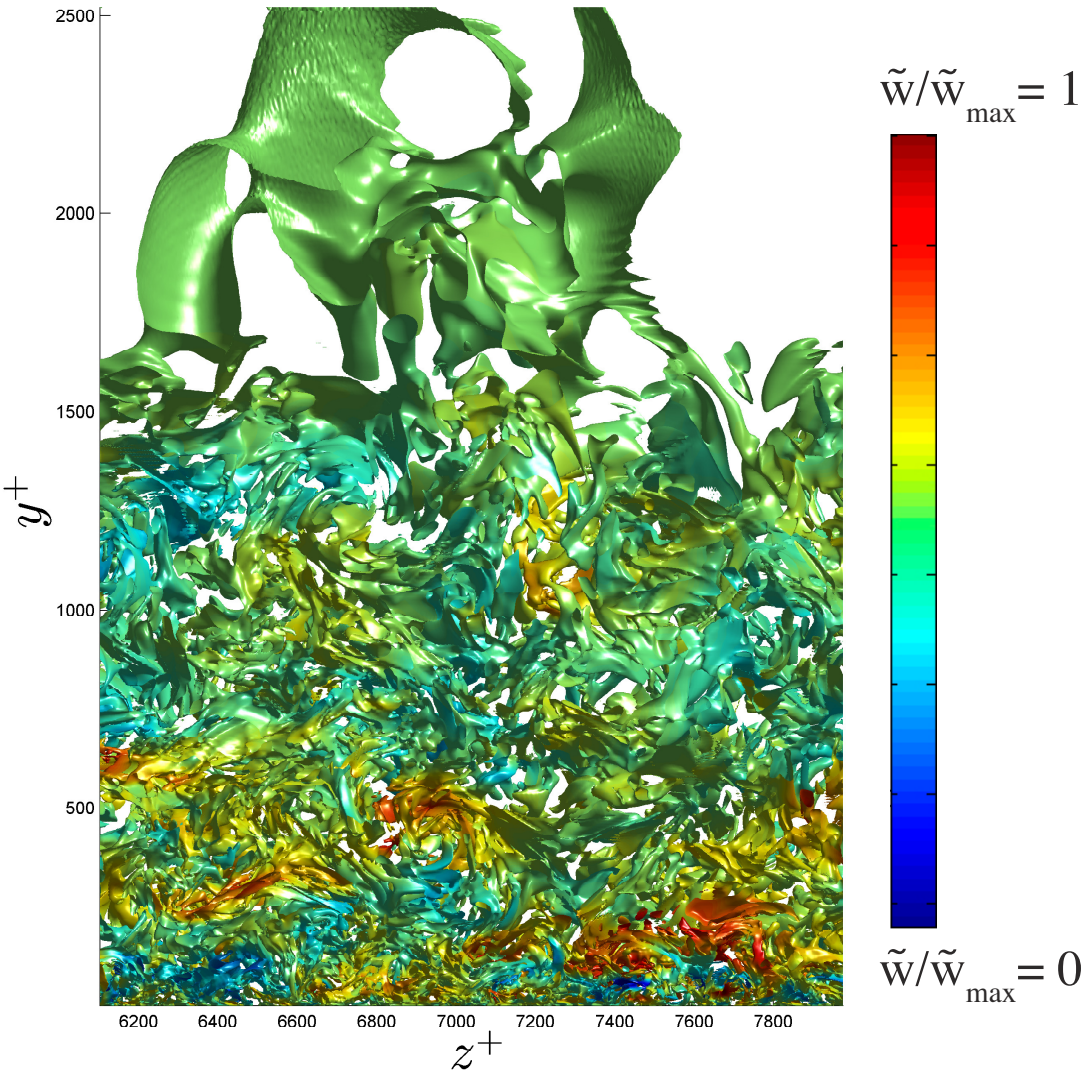

Figure 5.74: Streamwise view of the Q criterion isosurface colored by total spanwise velocity $\tilde{w}$ at $Re_\theta = 5200$

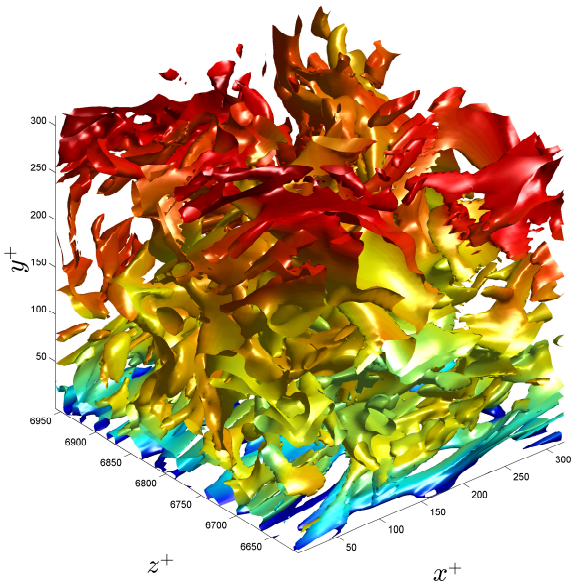

Figure 5.75: Near-wall ejection, zoomed-in view of Figure 5.71

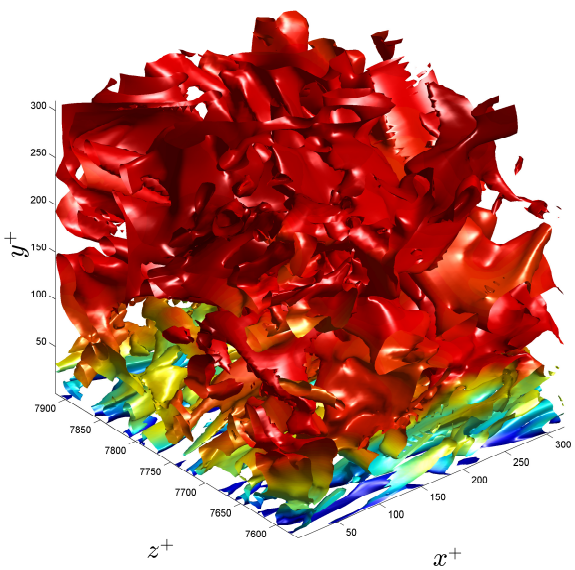

Figure 5.76: Near-wall sweep, zoomed-in view of Figure 5.71

Large-scale intermittent structures that are elongated in the streamwise direction are clearly seen in the wake region of Figures 5.71-5.72. The large structures extend from the buffer layer all the way to the outer edge of the boundary layer, in agreement with the observations of Schlatter *et al.*[82] Using a two-point correlation to examine the fluctuating wall shear stress, they found not only a peak associated with near wall streaks but also a peak associated with larger spanwise structures, roughly 0.85δ in size, for $Re_\theta > 1500$.

The turbulent boundary layer structure, visualized by the Q criterion at $Re_\theta = 4101$ and $Re_\theta = 5200$ in the BL_{6600} simulation of the UPM Fluid Dynamics Group, agrees with the qualitative description of the taxonomy of structures provided by Robinson.[1] In addition, large spanwise structures were visualized and identified as those predicted by Schlatter *et al.*[82] for $Re_\theta > 1500$. The result indicates that the hairpin vortices found by Wu & Moin[76] may be an artifact of low Reynolds number flows, specific turbulence trips, or both. This assertion is supported by isosurfaces of the DNS data generated by Schlatter & Örlü[58], which show hairpin vortices at low Reynolds numbers that break apart into a field of fragmented hairpin vortices by approximately $Re_\theta = 4000$. Furthermore, the smoke visualization by Head & Andreopoulos[75] is the only observational evidence of hairpin vortices and they observed that complete hairpins disappeared for $Re_\theta > 5000$.[70] It is important to note that the turbulence tripping mechanism influences the structure of the flow at low Reynolds number. Wu & Moin[76] note that the turbulence trip of Head & Andreopaulos is widely considered to have been too large to generate a canonical turbulent boundary layer, and they used a periodic puff of homogenous turbulence to sustain their simulated turbulent boundary layer instead of a turbulent inflow method. Schlatter & Örlü[83] examined the effect of different tripping devices used in DNS and found that the residual effects of the specific trip are observable in turbulent statistics up to $Re_\theta = 3000$.

Chapter 6

Conclusions

A complete database of third-, fourth-, and fifth-order central velocity moments in a turbulent boundary layer is presented. The profiles of fourth- and fifth-order moments constructed using Gram-Charlier procedure and the Millionshtchikov's quasi-normality hypothesis procedure approximate the behavior of the true fourth- and fifth-order moments. The maximum error for the constructed moments occurs in the inner region (the region of maximum production of turbulent kinetic energy), for moments that contain streamwise fluctuations. A source of error may be the slightly different locations of the peak streamwise moments, which alternate in the buffer layer between even- and odd-order moments. Since the two procedures explored in this thesis impose assumptions about the proximity of the probability distributions to Gaussian distribution, the Gaussianity or non-Gaussianity of individual moments may be an additional source of error.

The moment interrelations approximately agree, and since the approach is statistical, it is plausible that the approximate agreement will hold true for any flow of interest. However, more data from other benchmark flows should be collected and processed in the same manner to generate a clear picture of the universality of the

quality of the moment interrelations. Furthermore, it is not known if the moment interrelations improve with increasing Reynolds number. It has been shown previously by Poroseva[84] that conventional second-moment-closures that include empirical functions are increasingly accurate for increasing Reynolds numbers in rotating pipe flow. The same study also indicated that as the Reynolds number increases, the impact of empirical functions on the flow solution produced by conventional second-moment closures weakens. The primary conclusion of this thesis is that statistical procedures for constructing third- and higher-moment closure terms are broadly accurate enough to warrant implementation in second- and higher-order RANS closure schemes. Implementation, verification, and validation of new schemes based on the statistical procedures is needed.

The turbulent boundary layer structure visualized using Q criterion isosurfaces at $Re_\theta = 5200$ in the BL_{6600} simulation of the UPM Fluid Dynamics Group agrees with the description of the taxonomy of structures provided by Robinson[1] and with recent visualizations of the flow field by Schlatter & Örlü.[58] In addition, large scale structures on the order of the boundary layer thickness were visualized and identified as those predicted by Schlatter *et al.*[82] and also shown by Schlatter & Örlü[58] for $Re_\theta > 1500$. The large structures that extend down into the inner region are consistent with those described by Smits *et al.*[5]

References

[1] S.K. Robinson. Coherent motions in the turbulent boundary layer. *Annu. Rev. Fluid Mech.*, 23(1):601–639, 1991.

[2] O. Reynolds. On the dynamical theory of incompressible viscous fluids and the determination of the criterion. *Philos. Trans. R. Soc. Lond. A*, pages 123–164, 1895.

[3] S. B. Pope. *Turbulent Flows*. Cambridge University Press, 2000.

[4] P.S. Bernard and J.M. Wallace. *Turbulent Flow: Analysis, Measurement, and Prediction*. John Wiley & Sons Inc., 2002.

[5] A.J. Smits, B.J. McKeon, and I. Marusic. High-Reynolds number wall turbulence. *Annu. Rev. Fluid Mech.*, 43:353–375, 2011.

[6] F. Durst, J. Jovanović, and T.G. Johansson. On the statistical properties of truncated Gram-Charlier series expansions in turbulent wall-bounded flows. *Phys. Fluids*, 4(1):118–126, 1991.

[7] D.B. DeGraaff and J.K. Eaton. Reynolds number scaling of the flat-plate turbulent boundary layer. *J. Fluid Mech.*, 422:319–346, 2000.

[8] J. Jiménez, S. Hoyas, M.P. Simens, and Y. Mizuno. Turbulent boundary layers and channels at moderate Reynolds numbers. *J. Fluid Mech.*, 657:335–360, 2010.

[9] Kampé de Fériet. The Gram-Charlier approximation of the normal law and the statistical description of homogeneous turbulent flow near statistical equilibrium. No. 2013, Naval Ship Research and Development Center, Washington, D.C., 1966.

[10] M.D. Millionshtchikov. On the theory of homogeneous isotropic turbulence. *C. R. Acad. Sci. SSSR*, 32:615–619, 1941.

[11] P. Moin and K. Mahesh. Direct numerical simulation: A tool in turbulence research. *Annu. Rev. Fluid Mech.*, 30(1):539–578, 1998.

[12] A.N. Kolmogorov. Dissipation of energy in locally isotropic turbulence. *Dokl. Akad. Nauk SSSR*, 32(1):16–18, 1941.

[13] J.H. Ferziger and Perić. *Computational Methods for Fluid Dynamics*. Springer-Verlag, 2002.

[14] J. Kim and P. Moin. Application of a fractional-step method to incompressible Navier-Stokes equations. *J. Comp. Phys.*, 59(2):308–323, 1985.

[15] P.R. Spalart and A. Leonard. Direct numerical simulation of equilibrium turbulent boundary layers. In *Proceedings of the Fifth Symposium on Turbulent Shear Flows*, Ithaca, NY, 1985.

[16] T.S. Lund, X. Wu, and K.D. Squires. Generation of turbulent inflow data for spatially-developing boundary layer simulations. *J. Comp. Phys.*, 140(2):233–258, 1998.

[17] P. Saguat. *Large Eddy Simulation For Incompressible Flow*. 3^{rd} ed., Springer-Verlag, 2006.

[18] J.A. Sillero, J. Jiménez, and R.D. Moser. One-point statistics for turbulent wall-bounded flows at Reynolds numbers up to $\delta^+ = 2000$. *Phys. Fluids*, 25(10):1–15, 2013.

[19] J.M. Österlund. *Experimental Studies of Zero Pressure-Gradient Turbulent Boundary Layer Flow*. PhD thesis, Kungl Tekniska Hogskolan, Sweden, 1999.

[20] W.K. George and L. Castillo. Zero-pressure-gradient turbulent boundary layers. *Applied Mechanics Reviews*, 50(12):689–729, 1997.

[21] P.A. Monkewitz, K.A. Chauhan, and H.M. Nagib. Self-consistent high-Reynolds number asymptotics for zero-pressure-gradient turbulent boundary layers. *Phys. Fluids*, 19(11), 2007.

[22] R.L. Panton. Composite asymptotic expansions and scaling wall turbulence. *Phil. Trans. R. Soc. A., Math. Phys. Eng. Sci.*, 365:733–754, 2007.

[23] T. Wei, P. Fife, J. Klewicki, and P. McMurty. Properties of the mean momentum balance in turbulent boundary layer, pipe, and channel flows. *J. Fluid Mech.*, 522:303–327, 2005.

[24] S.C. Kassinos, C.A. Langer, G. Iaccarino, and P. Moin. *Complex Effects in LES*. Springer-Verlag, 2007.

[25] M. Germano, U. Piomelli, P. Moin, and W.H. Cabot. A dynamic subgrid-scale eddy viscosity model. *Phys. Fluids*, 3(7):1760–1765, 1991.

[26] A.S. Monin and A.M. Yaglom. *Statistical Fluid Mechanics: Mechanics of Turbulence*. The MIT Press, 1979.

[27] D.C. Wilcox. *Turbulence Modeling for CFD*. D.C.W. Industries, 1998.

[28] P.R. Spalart. Strategies for turbulence modeling and simulations. *Int. J. Heat Fluid Flow*, 21:252–263, 2000.

[29] S. Torii and W. Yang. Numerical prediction of fully-developed turbulent swirling flows in an axially rotating pipe by means of a modified $k-\epsilon$ turbulence model. *Int. J. Numer. Meth. Heat Fluid Flow*, 5:175–183, 1995.

[30] J. Jovanović, F. Durst, and T.G. Johansson. Statistical analysis of the dynamic equations for higher-order moments in turbulent wall-bounded flows. *Phys. Fluids*, 5(11):2886–2900, 1993.

[31] C.G. Speziale. Turbulence modeling for time-dependent RANS and VLES: A review. *AIAA J.*, 36(2), 1998.

[32] P.R. Spalart. Detached-eddy simulations. *Annu. Rev. Fluid Mech.*, 41:181–202, 2009.

[33] J. Sauer. *Towards Improved Capability and Confidence in Coupled Atmospheric and Wildland Fire Modeling.* PhD thesis, Florida State University, 2013.

[34] R.R. Linn, J.M. Canfield, P. Cunningham, C. Edminster, J.-L. Dupuy, and F. Pimont. Using periodic line fires to gain a new perspective on multi-dimensional aspects of forward fire spread. *Agricultural and Forest Meteorology*, 157:60–76, 2012.

[35] F. Pimont, J.-L. Dupuy, R.R. Linn, and S. Dupont. Validation of firetec wind-flows over a canopy and a fuel-break. *Intl. J. Wild. Fire*, 18:775–790, 2009.

[36] R.R. Linn and P. Cunningham. Numerical simulations of grass fires using a coupled atmosphere-fire model: Basic fire behavior and dependence on wind speed. *J. Geophysical Research*, 110:1–19, 2005.

[37] Schetz J.A. and Bowersox R.D.W. *Boundary Layer Analysis.* American Institute of Astronautics and Aeronautics, 2nd edition, 2002.

[38] S. Nagarajan, S.K. Lele, and J.H. Ferziger. A robust high-order compact method for large eddy simulation. *J. Comp. Phys.*, 191:329–419, 2003.

[39] Jiménez J. Hoyas S. Mizuno Y. Simens, M.P. A high-resolution code for turbulent boundary layers. *J. Comp. Phys.*, 228(11):4218–4231, 2009.

[40] F.H. Harlow and J.E. Welch. Numerical calculation of time-dependent viscous incompressible flow of fluid with a free surface. *Phys. Fluids*, 8(12):2182, 1965.

[41] G. Borrell, J.A. Sillero, and J. Jiménez. A code for direct numerical simulation of turbulent boundary layers at high Reynolds numbers in BG/P supercomputers. *Computers & Fluids*, 80:37–43, 2013.

[42] W.R. Schwarz. *Experiment and Modelling of a Three-Dimensional Turbulent Boundary Layer in a 30 Degree Bend*. PhD thesis, Department of Mechanical Engineering, Stanford University, 1992.

[43] B. Fornberg. Calculation of weights in finite difference formulas. *SIAM Rev.*, 40(3):685–691, 1998.

[44] G. Dahlquist and A. Björk. *Numerical Methods in Scientific Computing*. Society for Industrial and Applied Mathematics, 2008.

[45] J.L. Lumley. *Stochastic Tools in Turbulence*. 3^{rd} ed., Academic Press, New York, 1970.

[46] R.A. Antonia and J.D. Atkinson. High-order moments of Reynolds shear stress fluctuations in a turbulent boundary layer. *J. Fluid Mech.*, 58(3):581–593, 1973.

[47] F.N. Frenkiel and P.S. Klebanoff. Probability distributions and correlations in a turbulent boundary layer. *Phys. Fluids*, 16(6):727–737, 1973.

[48] H. Nakagawa and I. Nezu. Prediction of the contributions to the reynolds stress from bursting events in open-channel flows. *J. Fluid Mech.*, 58(3):581–593, 1977.

[49] V.I Bukreev, V.V. Zykov, and V.A. Kostomakha. One-dimensional probability distribution laws of velocity fluctuations in turbulent flow in a circular tube. *Izvestiia Sibirskogo Otdeleniia Akademii Nauk SSSR, Seriia Tekhnicheskikh Nauk*, 13(3), 1975. (in Russian).

[50] M.I. Pilipchuk. *A Study of Statistical Characteristics of the Longitudinal Velocity Component in a Turbulent Flow in a Rotating Pipe*. PhD thesis, Moscow Physico-Technical Institute, Russia, 1986. (in Russian).

[51] S.V. Poroseva. *High-Order Turbulence Closure in a Fully-Developed Flow in a Cylindrical Pipe*. PhD thesis, Novosibirsk State University, Russia, 1996.

[52] A.F. Kurbatskii and S.V. Poroseva. A model for calculating the three components of the excess for the turbulent flow velocity in a round pipe rotating about longitudinal axis. *High Temp.*, 35(3):432–440, 1997.

[53] M.S. Uberoi. Quadruple velocity correlations and pressure fluctuations in isotropic turbulence. *J. Aero. Sci*, 20(3):197–204, 1953.

[54] P.G. Zaets, A.T. Onufriev, M.I. Pilipchuk, and R.A. Safarov. Fourth-order two-point correlation functions for the longitudinal velocity in a turbulent flow in an axially rotating pipe. *VINITI*, 1984. (in Russian).

[55] D.B. DeGraaff. *Reynolds Number Scaling of the Turbulent Boundary Layer on a Flat Plate and on Swept and Unswept Bumps*. PhD thesis, Department of Mechanical Engineering, Stanford University, 1999.

[56] R.W. Smith. *Effect of Reynolds Number on the Structure of Turbulent Boundary Layers*. PhD thesis, Princeton University, 1994.

[57] J. Klewicki. *On the Interactions between Inner and Outer Region Motions in Turbulent Boundary Layers*. PhD thesis, Michigan State University, U.S.A., 1989.

[58] P. Schlatter and R. Örlü. Assessment of direct numerical simulation data of turbulent boundary layers. *J. Fluid Mech.*, 659:116–126, 2010.

[59] N. Hutchins and I. Marusic. Large-scale influences in near-wall turbulence. *Philos. Trans. R. Soc. Lond. A.*, 23:647–664, 2007.

[60] J. Murlis, H.M. Tasi, and P. Bradshaw. The structure of turbulent boundary layers at low reynolds numbers. *J. Fluid Mech.*, 122:13–56, 1982.

[61] C.R. Smith and S.P. Schwartz. Observation of streamwise rotation in the near-wall region of a turbulent boundary layer. *Phys. Fluids*, 26:641–652, 1983.

[62] S.J. Kline, W.C. Reynolds, F.A. Schraub, and P.W. Runstadler. The structure of turbulent boundary layers. *J. Fluid Mech.*, 30:741–773, 1967.

[63] Gupta A.K., J. Laufer, and R.E. Kaplan. Spatial structure in the viscous sublayer. *J. Fluid Mech.*, 50:493–512, 1971.

[64] H.T. Kim, S.J. Kline, and W.C. Reynolds. The production of turbulence near a smooth wall in a turbulent boundary layer. *J. Fluid Mech.*, 50:133–160, 1971.

[65] P.H. Alfredsson and A.W. Johansson. On the detection of turbulence-generating events. *J. Fluid Mech.*, 139:325–345, 1984.

[66] R.F. Blackwelder and L.S.G. Kovasznay. Time scales and correlations in a turbulent boundary layer. *Phys. Fluids*, 5:1011–1022, 1972.

[67] E.R. Corino and R.S. Brodkey. A visual investigation of the wall region in turbulent flow. *J. Fluid Mech.*, 37:1–30, 1967.

[68] H.P. Kreplin and H. Eckelmann. Behavior of the three fluctuation velocity components in the wall region of a turbulent channel flow. *Phys. Fluids*, 22(299):1233–1239, 1979.

[69] J.M. Wallace, H. Eckelmann, and R.S. Brodkey. The wall region in turbulent shear flow. *J. Fluid Mech.*, 54:39–48, 1972.

[70] A. Honkan and Y. Andreopoulos. Vorticity, strain-rate and dissipation characteristics in the near-wall region of turbulent boundary layers. *J. Fluid Mech.*, 250:29–06, 1997.

[71] M.H. Buschmann, T. Indinger, and M. Gad-el-Hak. Near-wall behavior of turbulent wall-bounded flows. *Int. J. Heat Fluid Flow*, 30(5):993–1006, 2009.

[72] M.S. Chong, A.E. Perry, and B.J. Cantwell. A general classification of three-dimensional flow fields. *Phys. Fluids*, 2:765–777, 1990.

[73] R. J. Adrian, C.D. Meinhart, and C.D. Tomkins. Vortex organization in the outer region of the turbulent boundary layer. *J. Fluid Mech.*, 422:1–54, 2000.

[74] C.D. Tomkins and R.J. Adrian. Spanwise structure and scale growth in turbulent boundary layers. *J. Fluid Mech*, 490:37–74, 2003.

[75] M.R. Head and P. Bandyopadhyay. New aspects of turbulent boundary layer structures. *J. Fluid Mech.*, 107:297–338, 1981.

[76] X. Wu and P. Moin. Direct numerical simulation of turbulence in a nominally zero-pressure-gradient flat-plate boundary layer. *J. Fluid Mech.*, 630:5–41, 2009.

[77] L.P. Erm and P.N. Joubert. Low-reynolds number turbulent boundary layers. *J. Fluid Mech.*, 230(299):1–44, 1991.

[78] P.S. Bernard, J.M. Thomas, and R.A. Handler. Vortex dynamics and the production of reynolds stress. *J. Fluid Mech.*, 253:385–419, 1993.

[79] G. Haller. An objective definition of a vortex. *J. Fluid Mech.*, 525:1–26, 2005.

[80] M. A. Green, C.W. Rowley, and G. Haller. Detection of Lagrangian coherent structures in three-dimensional turbulence. *J. Fluid Mech.*, 572:111–120, 2007.

[81] J.C. Hunt, A.A. Wray, and P. Moin. Eddies, streams, and convergence zones in turbulent flows. Ctr-2250, 1988.

[82] P. Schlatter, R. Örlü, Q. Li, G. Brethouwer, J.H.M. Fransson, A.V. Johansson, P.H. Alfredsson, and D.S. Henningson. Turbulent boundary layers up to $re_\theta = 2500$ studied through simulation and experiment. *Phys. Fluids*, 21:1–4, 2009.

[83] P. Schlatter and R. Örlü. Turbulent boundary layers at moderate reynolds numbers: Inflow length and tripping effects. *J. Fluid Mech.*, 710:5–34, 2012.

[84] S.V. Poroseva. The effect of a pressure-containing correlation model on near-wall flow simulations with reynolds stress transport models. *J. Fluid Eng.*, 138(6), 2013.

[85] P.H. Alfredsson, A. Segalini, and R. Örlü. A new scaling for the streamwise turbulence intensity in wall-bounded turbulent flows and what it tells us about the outer peak. *Phys. Fluids*, 23(4), 2011.

[86] K.A. Chauhan, P.A. Monkewitz, and H.M. Nagib. Criteria for assessing experiments in zero pressure gradient boundary layers. *Fluid Dyn. Res.*, 41:1–23, 2009.

[87] J. Jovanović. *Statistical Analysis and Structure of Wall Turbulence*. PhD thesis, Mechanical Engineering, University of Belgrade, Yugoslavia, 1984.